J Eng Math (2017) 107:201–230
DOI 10.1007/s10665-017-9914-x

Primary cementing of oil and gas wells in turbulent and mixed regimes

Amir Maleki · **Ian Frigaard**

Received: 3 April 2017 / Accepted: 29 May 2017 / Published online: 22 July 2017

Abstract We present a detailed derivation of a practical two-dimensional model for turbulent and mixed regimes in narrow annular displacement flows, such as are found during the primary cementing of oil and gas wells. Such mixed cross regimes, including those in which different regimes exist in the same annular cross section, are relatively common in primary cementing. The modelling approach considers scaling based on the disparity of length-scales, which allows a narrow-gap averaging approach to be effective. With respect to the momentum equations, the leading-order equations correspond to a turbulent shear flow in the direction of the modified pressure gradient. This leads to a nonlinear elliptic problem that is the natural extension of the laminar displacement model in Bittleston et al. (J Eng Math 43:229–253, 2002). The mass transport equations that model the miscible displacement are however quite different. To leading-order turbulence effectively mixes the fluids. Changes in concentrations within the annular gap arise due to the combined effects of advection with the mean flow, anisotropic Taylor dispersion (along the streamlines) and turbulent diffusivity. The diffusive and dispersive effects are modelled for fully turbulent and transitional flows following Maleki and Frigaard (J Non-Newt Fluid Mech 235:1–19, 2016). The model derived allows the investigation of different well geometries and inclinations, pumping sequences and fluid rheologies, all of which can have importance. A number of computed examples are presented with the aim of demonstrating the complexity of turbulent displacements.

Keywords Annular displacement · Dispersion · Primary cementing · Turbulent flow

1 Introduction

Primary cementing is the process by which oil and gas wells are sealed during construction. The seal is achieved by placing cement into a narrow gap formed between the drilled borehole and the outside of a steel casing (or liner) that is placed in the well. The cement not only seals the well hydraulically, preventing fluids from migrating axially

---

A. Maleki
Department of Mechanical Engineering, University of British Columbia, 2054-6250 Applied Science Lane,
Vancouver, BC V6T 1Z4, Canada

I. Frigaard (✉)
Department of Mathematics, University of British Columbia, 1984 Mathematics Road,
Vancouver, BC V6T 1Z2, Canada
e-mail: frigaard@math.ubc.ca

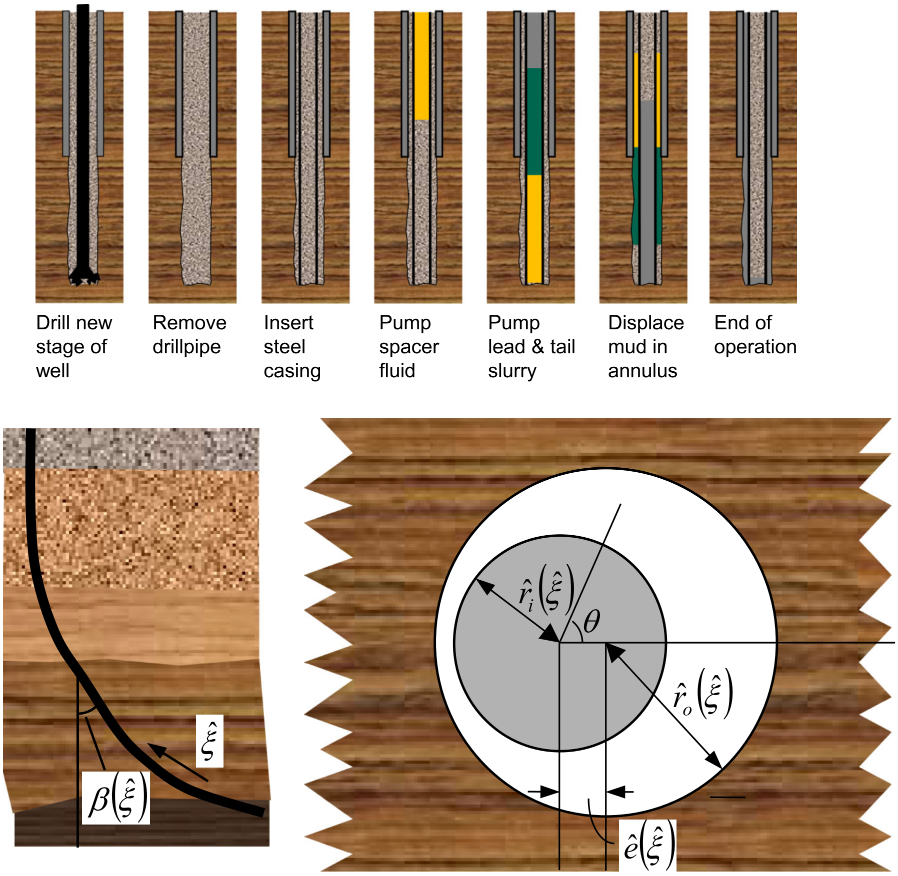

Fig. 1 Schematic of the well and of the variables that describe the eccentric annular geometry

along the wellbore between fluid-bearing zones, but also provides mechanical support, resisting geo-mechanical stresses. Failure to achieve proper zonal isolation can have significant effects on well productivity, as well as potential environmental and health consequences [1].

The process of placing the cement slurry into the narrow annular gap gives rise to a wide range of challenging fluid displacement problems, the understanding of which affects our ability to design wells of high integrity. This paper studies one class of flows commonly found, i.e., turbulent flows.

The primary cementing process proceeds as follows; see Fig. 1 (top). A new section of the well is drilled. The drillpipe is removed from the wellbore, leaving drilling mud inside the wellbore. A steel tube (casing or liner) is inserted into the wellbore, typically leaving an annular gap of ≈ 2 cm. The tubing is inserted in sections of length ≈ 10 m each, threaded together so that cemented sections can extend 100–1000 m. The so-called centralizers are fitted to the outside of the tube, to prevent the heavy steel tubing from slumping to the lower side of the wellbore. However, even in (nominally) vertical wells it is common that the annulus is eccentric and this is especially true in inclined and horizontal wells. With the steel casing in place and drilling mud on the inside and outside, the operation begins. First, the drilling mud is conditioned by circulating around the flow path. Next a sequence of fluids are circulated down the inside of the casing and returning up the outside of the annulus. Preflushes (washes or spacer fluids) are followed by one or more cement slurries. The fluid volumes are designed so that the cement slurries fill the annular space to be cemented. Drilling mud follows the final cement slurry to be pumped and the operations end with the cement slurry held in the annulus (with a valve system) and allowed to hydrate (i.e. set) over a period of many hours.

With reference to Fig. 1 (top), it can be seen that the completed well often has a telescopic arrangement of casings and liners.[1] Thus, the operation is repeated more than once on most wells. Typical, well inner diameters can start at anything up to 50 cm and can end as small as 10 cm in the producing zone. As the well proceeds deeper, pressures in fluid-bearing zones of the rock formation increase and must be balanced by the wellbore pressures in order to maintain *primary* well control. In deep or long wells the frictional component of the pressure can become significant. The need to control frictional pressures and these natural changes in annular geometry mean that the flow regimes experienced when cementing the surface casing (at the top) may be quite different from those found when cementing the production casing. As an example, in a long horizontal well drilled through a weak formation, one is likely to pump the fluids in laminar flow. Where adequate pump capacity is present and where there are no risks of either an influx nor fracturing the well, turbulent flow might be preferred.

This brings us to one of the main operational questions, which we will not succeed in answering here: is it preferable to cement a well in turbulent or laminar flow? There is a perception that turbulent regimes should be used where possible; see [1]. However, the actual evidence for this appears scant. For example, [2] is an often-cited study which does show improved displacement efficiencies. However, this study was performed in an era before our understanding of laminar displacements that evolved.

Laminar displacements allow fluid rheology and density differences to become part of the flow design. From the 1970s to early 1990s, a number of rule-based systems evolved to guide laminar mud displacement, e.g. [3–5]. For the past 10–20 years the industry has been able to access model-based simulators [6,7] and analyses [8,9] that have been shown to improve on the rule-based systems [10]. Such simulators are now actively used in cementing case studies, where they compare favourably with post-placement logging of the wells, e.g. [11–14]. Thus, early studies such as [2] have conclusions that may not be valid when instead comparing with modern designs for laminar displacement flows. Often operational or geological circumstances dictate the flow regime, so that it is rarely feasible in a field setting to cement one well in laminar flow and an identical adjacent well in turbulent flow. Herein lies the value of model-based simulations and laboratory experiments, where one can isolate individual effects. This paper derives the type of leading-order model tools that can be used to make such comparisons, over the scale of the well.

Our motivation for studying primary cementing stems from the important consequences of operational failure. Leakage during the primary cementing operation can lead to gas pockets and channels, that compromise the well. A number of other defects may arise either during the cementing of a well, or afterwards during cement hydration, that allow the well to leak later. The most common defects include: (a) residual mud channelling; (b) wet micro-annulus; (c) mixing/contamination of the slurry. Examples of these features can be found in [15]. Residual mud channelling is where the yield stress of the mud holds it in place (typically) on the narrow side of the annulus as preflushes and cement slurry by-pass. It is a bulk flow feature predicted well by simple mechanical arguments and more sophisticated models; see e.g. [6,16]. Wet micro-annulus is a local mechanical effect, where the displacing fluid does not generate sufficient shear stress to mobilize the mud at the wall. To some extent, this is predictable in model flows, e.g. [17–20], but can be further complicated with mud dehydration and uneven wellbores. Mixing (and consequent contamination) occur in different scenarios: downward displacement within the casing (e.g. [21,22]); fluid instabilities in laminar annular flows (e.g. [10,23,24]); turbulent annular displacement flows. In combination with mud channels, micro-annuli or even mud pockets left behind in irregular wellbores (e.g. washouts), residual drilling fluid can be partially eroded/dispersed in a passing slurry and continue to contaminate cement over long lengths.

While the above mechanisms are flow related and reflect our own interest, not all wellbore leakage has a fluid-mechanical cause. A good overview is given in [1], e.g. geomechanical stresses/deformation and casing de-bonding (=dry micro-annulus). The net summary is that many wells leak and this is common worldwide, although there is wide variation in cement evaluation techniques, regulatory practice, collection of (and access to) well data, and definition of leakage severity. For example, Dusseault et al. [25] state that over 550,000 wells have been drilled in Canada and collates survey data that show between 5–20% of wells with some form of leakage. The interested reader is also referred to [26,27], which analyze different leakage factors for significant datasets.

---

[1] A liner is a casing that extends downwards from just above the previous casing.

This paper concentrates on model development. Although we target turbulent flows, we also incorporate previous models for laminar flow regimes, e.g. [6], so that mixed flow regimes can be modelled. Flow regime depends on local geometry and fluid properties as well as the overall imposed flow rate. It is relatively common within the annulus that one fluid can be fully turbulent (e.g. a chemical wash or low-viscous spacer) while others are laminar. Indeed, this also can occur on a single section of the annulus, e.g. turbulent on the wide side, laminar or even static on the narrow side, (see later and [1]). Furthermore, although some fluids can be strongly turbulent, the more viscous fluids (muds, viscous spacers and slurries) are often only in weakly turbulent, transitional or laminar regimes. These flow regimes have become more prevalent in recent decades as extended and horizontal wells, require reduced flow rates to control friction pressures.

The organization of the paper is as follows: In Sect. 2, we derive an elliptic equation that models the stream function, for a given concentration field. Section 3 develops an asymptotic analysis to find the equation governing the leading-order evolution of the fluid concentrations. The model is summarized in Sect. 4, where we present examples of displacement flows with the increasing levels of complexity. The paper is closed in Sect. 5 with conclusions. Two appendices present, firstly, an overview of turbulent closure models used, and secondly, variational analysis that is preliminary to qualitative study, e.g. existence and uniqueness of weak solutions.

2 Modelling turbulent displacement flows

As in [6], a cylindrical coordinate system $(\hat{r}, \theta, \hat{\xi})$ is used to describe the well geometry: $\hat{\xi}$ measures distance along the central axis of the casing $\hat{r} = 0$ which is assumed to be inclined to the vertical with angle $\beta(\hat{\xi})$. The local cross section of the well, outside the casing, is assumed to be that of an eccentric annulus, with inner radius $\hat{r}_i(\hat{\xi})$, equal to the outer radius of the casing and outer radius $\hat{r}_o(\hat{\xi})$ equal to the inner radius of the hole (or previous casing). At each depth $\hat{\xi}$, the mean radius $\hat{r}_a(\hat{\xi})$ and the mean half-gap width $\hat{d}(\hat{\xi})$ are defined by

$$\hat{r}_a(\hat{\xi}) \equiv \frac{1}{2}\left[\hat{r}_o(\hat{\xi}) + \hat{r}_i(\hat{\xi})\right], \quad \hat{d}(\hat{\xi}) \equiv \frac{1}{2}\left[\hat{r}_o(\hat{\xi}) - \hat{r}_i(\hat{\xi})\right]. \tag{1}$$

Inner and outer radii, and the distance, $\hat{e}(\hat{\xi})$, between the two centres of the cylinders are given, see Fig. 1 (lower). It is assumed that $\hat{e}(\hat{\xi}) < 2\hat{d}(\hat{\xi})$ (the cylinders do not touch), and that variations in the geometry with $\hat{\xi}$ are *slow*. For simplicity, it is also assumed that the narrow side of the annulus will be found on the lower side of the well and that the casing remains stationary. Both these assumptions can be relaxed with care, e.g. [28,29].

The annular displacement is modelled as a concentration dependent multi-fluid flow that is fully turbulent and incompressible. The fluid constituents contribute to the *mixture* density $\hat{\rho}$ and to the rheological properties of the mixture. The latter are used in closure expressions that define the deviatoric stress tensor $\hat{\tau}_{ij}$. In primary cementing, a sequence of K fluids is pumped around the flow path, from the bottom of the annulus to the top. A typical sequence would be mud, wash, spacer, lead slurry, tail slurry and mud. When circulating, drilling muds, spacer fluids and cement slurries are predominantly shear thinning, nonlinearly viscous, and inelastic, often also with a significant yield stress. Washes are Newtonian fluids. In general, each constituent fluid can be effectively modelled as a Herschel-Bulkley fluid. We shall address evolution of the mixture concentrations at length in Sect. 3; however, for the present, we assume that all fluid properties are approximated effectively by closures that depend on the local mean fluid concentrations: both ensemble averaged and averaged across the annular gap.

We adopt the usual Reynolds decomposition for turbulent flows, into mean and fluctuating parts. Because the flows will be time-varying as the displacement proceeds, the mean part (denoted with an overbar below) is interpreted as an ensemble average. The velocity and pressure are $\hat{\mathbf{u}} = (\hat{u}, \hat{v}, \hat{w})$ and $\hat{p}$, respectively. In the local coordinate system, the Reynolds-decomposed Navier–Stokes system is

$$\frac{\partial}{\partial \hat{t}}\left[\hat{\rho}\bar{\hat{u}}\right]+\hat{\nabla}\cdot\left[\hat{\rho}\bar{\hat{u}}\bar{\hat{\mathbf{u}}}\right]=\frac{1}{\hat{r}}\frac{\partial}{\partial \hat{r}}\left[\hat{r}\bar{\hat{\tau}}_{\hat{r}\hat{r}}\right]+\frac{1}{\hat{r}}\frac{\partial}{\partial \theta}\bar{\hat{\tau}}_{\hat{r}\theta}+\frac{\partial}{\partial \hat{\xi}}\hat{\tau}_{\hat{r}\hat{\xi}}-\frac{\bar{\hat{\tau}}_{\theta\theta}}{\hat{r}}-\frac{\partial \bar{\hat{p}}}{\partial \hat{r}}+\hat{\rho}\hat{g}_{\hat{r}}$$
$$+\frac{1}{\hat{r}}\frac{\partial}{\partial \hat{r}}\left[\hat{r}\hat{\tau}^{t}_{\hat{r}\hat{r}}\right]+\frac{1}{\hat{r}}\frac{\partial}{\partial \theta}\hat{\tau}^{t}_{\hat{r}\theta}+\frac{\partial}{\partial \hat{\xi}}\hat{\tau}^{t}_{\hat{r}\hat{\xi}}-\frac{\hat{\tau}^{t}_{\theta\theta}}{\hat{r}}, \tag{2}$$

$$\frac{\partial}{\partial \hat{t}}\left[\hat{\rho}\bar{\hat{v}}\right]+\hat{\nabla}\cdot\left[\hat{\rho}\bar{\hat{v}}\bar{\hat{\mathbf{u}}}\right]=\frac{1}{\hat{r}^2}\frac{\partial}{\partial \hat{r}}\left[\hat{r}^2\bar{\hat{\tau}}_{\theta\hat{r}}\right]+\frac{1}{\hat{r}}\frac{\partial}{\partial \theta}\bar{\hat{\tau}}_{\theta\theta}+\frac{\partial}{\partial \hat{\xi}}\bar{\hat{\tau}}_{\theta\hat{\xi}}-\frac{1}{\hat{r}}\frac{\partial \bar{\hat{p}}}{\partial \theta}+\hat{\rho}\hat{g}_{\theta}$$
$$+\frac{1}{\hat{r}^2}\frac{\partial}{\partial \hat{r}}\left[\hat{r}^2\hat{\tau}^{t}_{\theta\hat{r}}\right]+\frac{1}{\hat{r}}\frac{\partial}{\partial \theta}\hat{\tau}^{t}_{\theta\theta}+\frac{\partial}{\partial \hat{\xi}}\hat{\tau}^{t}_{\theta\hat{\xi}} \tag{3}$$

$$\frac{\partial}{\partial \hat{t}}\left[\hat{\rho}\bar{\hat{w}}\right]+\hat{\nabla}\cdot\left[\hat{\rho}\bar{\hat{w}}\bar{\hat{\mathbf{u}}}\right]=\frac{1}{\hat{r}}\frac{\partial}{\partial \hat{r}}\left[\hat{r}\bar{\hat{\tau}}_{\hat{\xi}\hat{r}}\right]+\frac{1}{\hat{r}}\frac{\partial}{\partial \theta}\bar{\hat{\tau}}_{\hat{\xi}\theta}+\frac{\partial}{\partial \hat{\xi}}\bar{\hat{\tau}}_{\hat{\xi}\hat{\xi}}-\frac{\partial \bar{\hat{p}}}{\partial \hat{\xi}}+\hat{\rho}\hat{g}_{\hat{\xi}}$$
$$+\frac{1}{\hat{r}}\frac{\partial}{\partial \hat{r}}\left[\hat{r}\hat{\tau}^{t}_{\hat{\xi}\hat{r}}\right]+\frac{1}{\hat{r}}\frac{\partial}{\partial \theta}\hat{\tau}^{t}_{\hat{\xi}\theta}+\frac{\partial}{\partial \hat{\xi}}\hat{\tau}^{t}_{\hat{\xi}\hat{\xi}}, \tag{4}$$

$$0=\frac{1}{\hat{r}}\frac{\partial}{\partial \hat{r}}\left[\hat{r}\bar{\hat{u}}\right]+\frac{1}{\hat{r}}\frac{\partial \bar{\hat{v}}}{\partial \theta}+\frac{\partial \bar{\hat{w}}}{\partial \hat{\xi}}. \tag{5}$$

The components $\bar{\hat{\tau}}_{ij}$ are those that come from ensemble averages of the viscous stress tensor (which itself is nonlinear). The components $\hat{\tau}^{t}_{ij}$ are the turbulent (Reynolds) stresses, resulting from the fluctuating components of the velocity field $\hat{\mathbf{u}}'$, defined as

$$\hat{\tau}^{t}_{ij}=-\hat{\rho}\overline{\hat{u}'_i\hat{u}'_j}. \tag{6}$$

The gravitational acceleration, $\hat{\mathbf{g}}=(\hat{g}_{\hat{r}},\hat{g}_{\theta},\hat{g}_{\hat{\xi}})$, is given by

$$\hat{g}_{\hat{r}}=-\hat{g}\sin\beta(\hat{\xi})\cos\theta,\quad \hat{g}_{\theta}=\hat{g}\sin\beta(\hat{\xi})\sin\theta,\quad \hat{g}_{\hat{\xi}}=-\hat{g}\cos\beta(\hat{\xi}), \tag{7}$$

where $\hat{g}=9.81\ \mathrm{m/s^2}$.

2.1 Scaling and simplification

We wish to reduce our model to something more tractable than (2)–(5), by exploiting the aspect ratio of the annulus. The annulus geometry is typically long and narrow, with the typical gap half-width (∼1 cm) being much smaller than a typical azimuthal distance (∼30 cm), which in turn is much smaller than a typical length of the annulus (∼500 m).

Following [6], let the mean radius ($\hat{r}_{a,0}$), the local and global aspect ratios ($\delta(\hat{\xi})$ and δ_0 respectively) be defined by

$$\hat{r}_{a,0}=\frac{1}{\hat{Z}}\int_{\hat{\xi}_{bh}}^{\hat{\xi}_{tz}}\hat{r}_a(\hat{\xi})\,\mathrm{d}\hat{\xi},\quad \delta(\hat{\xi})=\frac{\hat{d}(\hat{\xi})}{\hat{r}_a(\hat{\xi})},\quad \delta_0=\frac{1}{\hat{Z}}\int_{\hat{\xi}_{bh}}^{\hat{\xi}_{tz}}\delta(\hat{\xi})\,\mathrm{d}\hat{\xi}. \tag{8}$$

where $\hat{Z}$ is the length of the zone of the well to be cemented, extending upwards from bottom hole, $\hat{\xi}_{bh}$, to the top of the zone, $\hat{\xi}_{tz}$. Scaled axial and azimuthal coordinates ξ and ϕ are then

$$\xi=\frac{\hat{\xi}-\hat{\xi}_{bh}}{\pi\hat{r}_{a,0}},\quad \phi=\frac{\theta}{\pi}. \tag{9}$$

In each cross section, we define the local average radius, $r = r_a(\xi)$, and local annulus eccentricity, $e(\xi)$, by

$$r_a(\xi) = \frac{\hat{r}_a(\hat{\xi})}{\hat{r}_{a,0}}, \quad e(\xi) = \frac{\hat{e}(\hat{\xi})}{2\hat{d}(\hat{\xi})}. \tag{10}$$

The centreline of the annular gap is at $\hat{r} = \hat{r}_{a,0} r_a(\xi) r_c(\phi, \xi)$. The radial coordinate is scaled relative to the distance from the centreline of the annulus, as follows:

$$y = \frac{\hat{r} - \hat{r}_{a,0} r_a(\xi) r_c(\phi, \xi)}{\hat{r}_{a,0}\delta_0}, \tag{11}$$

i.e. y is a local annular gap coordinate.

We assume a narrow annulus approximation: $\delta(\xi) \sim \delta_0 \ll \pi$; noting that δ_0/π, denotes the ratio of radial (gap) length-scales to azimuthal length-scale. To leading order in δ_0/π, we have $r_c(\phi, \xi) \sim 1$ and find that the inner and outer walls are at $y = \mp H(\phi, \xi)$, where

$$H(\phi, \xi) = \frac{\delta(\xi) r_a(\xi)[1 + e(\xi)\cos \pi\phi]}{\delta_0}. \tag{12}$$

More complex geometries are readily accommodated by specifying any $H(\phi, \xi)$ of $O(1)$ that varies slowly with ξ, e.g. $H(\phi - \phi_0(\xi), \xi)$ with H as above, retains the eccentric annular shape but shifts the wide side of the annulus to $\phi = \phi_0(\xi)$. Helically varying well eccentricity, elliptic cross sections and irregular washouts are each fairly common deviations away from (12).

Time is scaled with an advective timescale: $\pi\hat{r}_{a,0}/\hat{\hat{W}}$ where $\hat{\hat{W}}$ is representative of a mean axial velocity. For simplicity, we assume that the fluids are pumped following a schedule of pump rates: $\hat{Q}_{\text{pump}}(\hat{t})$, typically a step function. The pump schedule is used to define a representative flow rate $\hat{Q}_0$, e.g. the maximum flow rate. The mean axial velocity is $\hat{\hat{W}} = \hat{Q}_0/\hat{A}_0$, where $\hat{A}_0 = 4\pi\delta_0[\hat{r}_{a,0}]^2$ is a typical cross-sectional area of the annulus.

We now consider the relative sizes of the different terms in (2)–(5), with a view to simplification. Given that $\delta_0/\pi \ll 1$, we may assume that the dominant components of mean velocity will be in the (ϕ, ξ)-directions, scaling approximately with $\hat{\hat{W}}$. The incompressibility condition (5) suggests that the radial component of mean velocity scales with $\delta_0\hat{\hat{W}}/\pi$. Therefore, we can see that the acceleration and inertial terms on the left-hand side of (2), (3) and (4) have respective sizes:

$$\frac{\delta_0}{\pi}\frac{\hat{\rho}\hat{\hat{W}}^2}{\pi\hat{r}_{a,0}}, \qquad \frac{\hat{\rho}\hat{\hat{W}}^2}{\pi\hat{r}_{a,0}}, \qquad \frac{\hat{\rho}\hat{\hat{W}}^2}{\pi\hat{r}_{a,0}}.$$

Simplifying the stress terms on the right-hand side of (2), (3) and (4) is less straightforward. A number of authors have computed turbulent flows of Newtonian fluids in uniform eccentric annuli and calculated the Reynolds stresses, e.g. [30–33]. Here insofar as we are concerned, the main point is that each component of $\hat{\tau}^t_{ij}$ has similar magnitude, because the fluctuating velocity is inherently three-dimensional. In considering the viscous stresses, we need to consider two regions separately: the turbulent core of the annular flow and the wall region. In the turbulent core, the mean viscous stresses $\bar{\hat{\tau}}_{ij}$, are the average of the viscous stress and not the viscous stress of the averaged strain rate. Although the strain rate associated with the mean velocity can be estimated using scaling arguments, the fluctuating velocity also contributes to each component of the strain rate and indeed this contribution may be dominant in the core. Nonlinearity of the constitutive relations together with the probabilistic nature of the strain rate tensor prevents any easy simplification. A nice discussion may be found in [34, Chaps. 4 and 5]. All that we assume here is that the viscous stress components in the core all have similar magnitude, say $\bar{\hat{\tau}}_{ij} \sim \hat{\tau}_{\nu,0}$ for some viscous stress scale $\hat{\tau}_{\nu,0}$.

Conventionally, the Reynolds stresses in the turbulent core have similar size to the wall shear stresses (which will vary azimuthally in an eccentric annulus). In the wall region, the Reynolds stresses vanish, and the viscous stresses increase over a thin layer to match the wall shear stress. In this wall region, it is possible to estimate relative sizes of the different shear rates and approximate the flow. Thus, both turbulent and viscous stresses have roles to play in describing these flows. This is particularly true in cementing flows which are generally not highly turbulent, with the exception of low viscosity washes. For the present, we adopt a stress scale $\hat{\tau}_0$ that we apply to mean turbulent and viscous stresses, and discuss the order of magnitudes of dimensionless terms in different flow regimes later.

Next we consider the gravitational terms. It is common to exploit density differences in creating buoyancy forces to aid in displacing the in-situ drilling mud. To capture this aspect, we scale all densities with the density $\hat{\rho}_1$ of the first fluid in the pumping sequence, i.e. the in-situ drilling mud, and subtract the hydrostatic pressure from $\bar{\hat{p}}$. It is assumed that the pressure remaining balances the dominant stress gradients: $\bar{\hat{p}} = \bar{\hat{p}}_{bh}(\hat{t}) + \hat{\rho}_1 \mathbf{g} \cdot \mathbf{x} + (\pi \hat{\tau}_0/\delta_0)\bar{p}$, where $\bar{\hat{p}}_{bh}(\hat{t})$ denotes the bottom-hole pressure.

We now substitute the above variables into (2), (3) and (4) and divide through by the largest dimensional scales, to give the following.

$$\underbrace{O\left(\frac{\delta_0^3}{\pi^3}\frac{\hat{\rho}\hat{\bar{W}}^2}{\hat{\tau}_0}\right)}_{IT} = -\frac{\partial \bar{p}}{\partial y} + \underbrace{O\left(\frac{\delta_0}{\pi}\frac{\rho - 1}{Fr^2}\right)}_{BT} + \underbrace{O\left(\frac{\delta_0}{\pi}\right)}_{ST} + \underbrace{O\left(\frac{\delta_0}{\pi}\right)}_{CT}, \tag{13}$$

$$\underbrace{O\left(\frac{\delta_0}{\pi}\frac{\hat{\rho}\hat{\bar{W}}^2}{\hat{\tau}_0}\right)}_{IT} = -\frac{1}{r_a}\frac{\partial \bar{p}}{\partial \phi} + \frac{(\rho - 1)\sin\beta \sin \pi\phi}{Fr^2} + \frac{\partial}{\partial y}[\tau^t_{\phi y} + \bar{\tau}_{\phi y}] + \underbrace{O\left(\frac{\delta_0}{\pi}\right)}_{ST} + \underbrace{O\left(\frac{\delta_0}{\pi}\right)}_{CT}, \tag{14}$$

$$\underbrace{O\left(\frac{\delta_0}{\pi}\frac{\hat{\rho}\hat{\bar{W}}^2}{\hat{\tau}_0}\right)}_{IT} = -\frac{\partial \bar{p}}{\partial \xi} - \frac{(\rho - 1)\cos\beta}{Fr^2} + \frac{\partial}{\partial y}[\tau^t_{\xi y} + \bar{\tau}_{\xi y}], + \underbrace{O\left(\frac{\delta_0}{\pi}\right)}_{ST} + \underbrace{O\left(\frac{\delta_0}{\pi}\right)}_{CT}, \tag{15}$$

$$0 = \frac{\partial \bar{u}}{\partial y} + \frac{1}{r_a}\frac{\partial \bar{v}}{\partial \phi} + \frac{\partial \bar{w}}{\partial \xi} + \underbrace{O\left(\frac{\delta_0}{\pi}\right)}_{CT}, \tag{16}$$

where ρ is the scaled density and Fr is the Froude number:

$$Fr = \sqrt{\frac{\hat{\tau}_0}{\hat{\rho}_1 \hat{g} \delta_0 \hat{r}_{a,0}}}.$$

Our leading-order model is the narrow gap limit, $\delta_0/\pi \to 0$, with other parameters fixed. The different terms that will vanish in this limit are identified by the under-braces as follows: IT denote the leading-order inertial terms; BT denotes the next order buoyancy terms; ST denote the next order stress terms (turbulent and viscous); CT denote terms associated with curvature.

If the flow is fully turbulent, the stress scale $\hat{\tau}_0$ is the wall shear stress, so the ratio $\hat{\rho}\hat{\bar{W}}^2/\hat{\tau}_0$ that appears in the IT under-braces is effectively $\sim 1/f_f$, for a representative turbulent friction factor f_f. Although multiplied by

δ_0/π and formally vanishing in the narrow gap limit, these are likely to be the next largest terms. In the case that the flow is laminar, the Reynolds stress terms vanish, and the expression $\hat{\rho}\hat{\bar{\bar{W}}}^2/\hat{\tau}_0$ becomes effectively the Reynolds number, since in this case $\hat{\tau}_0$ is correctly interpreted as a viscous stress scale. Taking $\delta_0/\pi \to 0$ leads to the laminar displacement model of [6].

The curvature terms arise both due to replacing the r-derivativesmarizewith y-derivatives (changing $1/r$ to $1/r_a + O(\delta_0/\pi)$), and due to slow variations in ξ as the well trajectory changes (assumed of $O(\delta_0/\pi)$). The next order stress terms are also only $O(\delta_0/\pi)$ smaller in the turbulent flow: from scaling, using the geometric aspect ratio, i.e. the partial derivatives are smaller in the (ϕ, ξ)-plane than with respect to y. If the flow were laminar, then the Reynolds stresses would vanish and scaling arguments can be used to estimate the size of the viscous stresses; the next largest stresses appear at $O((\delta_0/\pi)^2)$.

To summarize, if we consider the next order terms we see that there is a proliferation of terms at order δ_0/π: buoyancy terms, inertial, stress and curvature. The main point here is that to include the next order of terms in δ_0/π is prohibitively complex. On the other hand, considering the formal narrow gap limit, $\delta_0/\pi \to 0$, although the scaling arguments are different the leading-order equations are similar to those of [6].

2.2 Narrow gap approximation

Proceeding with the narrow gap approximation, we take $\delta_0/\pi \to 0$ in (13)–(16). To eliminate $\bar{u}$, we integrate (16) across the gap width, using conditions of no-slip at the annulus walls:

$$\frac{\partial}{\partial \phi}[2H\bar{\bar{v}}] + \frac{\partial}{\partial \xi}[2r_a H\bar{\bar{w}}] = 0, \tag{17}$$

where

$$\bar{\bar{v}}(\phi, \xi, t) = \frac{1}{2H}\int_{-H}^{H} \bar{v}\,\mathrm{d}y, \quad \bar{\bar{w}}(\phi, \xi, t) = \frac{1}{2H}\int_{-H}^{H} \bar{w}\,\mathrm{d}y. \tag{18}$$

Equation (17) is satisfied using a stream function:

$$2r_a H\bar{\bar{w}} = \frac{\partial \Psi}{\partial \phi}, \quad 2H\bar{\bar{v}} = -\frac{\partial \Psi}{\partial \xi}. \tag{19}$$

For later convenience, we introduce 2D annular divergence and gradient operators as follows:

$$\nabla_a \cdot \mathbf{q} = \frac{1}{r_a}\frac{\partial q_\phi}{\partial \phi} + \frac{\partial q_\xi}{\partial \xi}, \qquad \nabla_a q = \left(\frac{1}{r_a}\frac{\partial q}{\partial \phi}, \frac{\partial q}{\partial \xi}\right).$$

Turning now to the momentum balance, from (13) we see the pressure is independent of y, as is ρ (see below in Sect. 3). Equations (14) and (15) may be integrated across the annular gap, assuming symmetry at $y = 0$ for this leading-order approximation:

$$\left(\tau^t_{\phi y} + \bar{\tau}_{\phi y}, \tau^t_{\xi y} + \bar{\tau}_{\xi y}\right) = y\left(\frac{1}{r_a}\frac{\partial \bar{p}}{\partial \phi} - \frac{(\rho - 1)\sin\beta\sin\pi\phi}{Fr^2}, \frac{\partial \bar{p}}{\partial \xi} + \frac{(\rho - 1)\cos\beta}{Fr^2}\right). \tag{20}$$

The leading-order stresses are only non-zero in the direction of the modified pressure gradient. Viewed in the (ϕ, ξ)-plane, this is a one-dimensional (1D) turbulent shear flow through a channel of width $2H(\phi, \xi)$, driven in the direction of

$$-\left(\frac{1}{r_a}\frac{\partial \bar{p}}{\partial \phi} - \frac{(\rho - 1)\sin\beta\sin\pi\phi}{Fr^2}, \frac{\partial \bar{p}}{\partial \xi} + \frac{(\rho - 1)\cos\beta}{Fr^2}\right),$$

which is therefore also the direction of the streamlines, say $\mathbf{e}_s$:

$$\mathbf{e}_s = \frac{(\bar{\bar{v}}, \bar{\bar{w}})}{\sqrt{\bar{\bar{v}}_0^2 + \bar{\bar{w}}_0^2}} = \frac{1}{|\nabla_a \Psi|}\left(-\frac{\partial \Psi}{\partial \xi}, \frac{1}{r_a}\frac{\partial \Psi}{\partial \phi}\right). \tag{21}$$

The integrated momentum balance (20) can now be resolved along the streamlines, in the $\mathbf{e}_s$ direction:

$$\tau_{sy}^t + \bar{\tau}_{sy} = -\frac{y}{H}\tau_w, \tag{22}$$

where the dimensionless wall shear stress τ_w is:

$$\tau_w = H\left|\left(\frac{1}{r_a}\frac{\partial \bar{p}}{\partial \phi} - \frac{(\rho-1)\sin\beta\sin\pi\phi}{Fr^2}, \frac{\partial \bar{p}}{\partial \xi} + \frac{(\rho-1)\cos\beta}{Fr^2}\right)\right|. \tag{23}$$

In [35], we solved (22) to give an expression for the leading-order turbulent mean velocity for a Herschel–Bulkley fluid, based on the phenomenological approach of Metzner–Reed–Dodge [36–38]. For the purposes of our model, we simply note that [35] provides a closure expression $\tau_w = \tau_w(|\nabla_a \Psi|; \phi, \xi, t)$. The local dependency (ϕ, ξ) explicitly reflects the local geometric variables, and the fluid rheology is represented implicitly with dependency (ϕ, ξ, t) as the fluids are displaced; see Appendix A.

Combining (21) and (23), we have

$$\frac{1}{|\nabla_a \Psi|}\left(-\frac{\partial \Psi}{\partial \xi}, \frac{1}{r_a}\frac{\partial \Psi}{\partial \phi}\right) = -\frac{H}{\tau_w}\left(\frac{1}{r_a}\frac{\partial \bar{p}}{\partial \phi} - \frac{(\rho-1)\sin\beta\sin\pi\phi}{Fr^2}, \frac{\partial \bar{p}}{\partial \xi} + \frac{(\rho-1)\cos\beta}{Fr^2}\right), \tag{24}$$

which can be rearranged and cross-differentiated to eliminate the pressure:

$$\nabla_a \cdot [\mathbf{S} + \mathbf{b}] = 0 \tag{25}$$

in which

$$\mathbf{S} = \frac{r_a \tau_w(|\nabla_a \Psi|)}{H|\nabla_a \Psi|}\nabla_a \Psi \quad \text{and} \quad \mathbf{b} = \frac{r_a(\rho-1)}{Fr^2}(\cos\beta, \sin\pi\phi\sin\beta). \tag{26}$$

The term $\nabla_a \cdot \mathbf{S}$ in (25) is a quasilinear elliptic operator on Ψ and the term $\nabla_a \cdot \mathbf{b}$ provides a source term that is driven by the spatial gradients of the buoyancy vector $\mathbf{b}$. Note that (25) contains no time derivatives: time enters only via (i) boundary data, e.g. if the flow rate changes; (ii) through the fluid concentrations, which affect both fluid rheology and buoyancy.

Note that we have still not fixed the shear stress scale $\hat{\tau}_0$, and this is not particularly important as all terms in (25) are scaled with $\hat{\tau}_0$. Although this paper has targeted turbulent flows in terms of the novel contribution to modelling of primary cementing, laminar flows are more prevalent. The scale $\hat{\rho}_1 \hat{\bar{W}}^2$ also over-estimates the turbulent stresses (by using the mean velocity and not a friction velocity), and these in turn are larger than the typical laminar viscous stresses. In addition, the objective has been to develop a model capable of dealing with mixed flow regimes. Consequently, we define a $\hat{\tau}_0$ that is relevant to the laminar viscous stresses:

$$\hat{\tau}_0 = \max_k\left\{\hat{\tau}_{k,Y} + \hat{\kappa}_k \hat{\dot{\gamma}}_0^{n_k}\right\}, \qquad \hat{\dot{\gamma}}_0 = \frac{3\hat{\bar{W}}}{\delta_0 \hat{r}_{a,0}}, \tag{27}$$

with $\hat{\tau}_{k,Y}$, $\hat{\kappa}_k$, and n_k, respectively the yield stress, consistency and power-law index of fluid k in the pumped sequence. Using this scale we define the functions $\tau_w(|\nabla_a \Psi|)$ and $\mathbf{S}$, by using the closure expressions in [35], as outlined in Appendix A.

2.2.1 Boundary conditions

The elliptic second order equation (25) determines the stream function, and hence gap-averaged velocity, at each time. It requires suitable boundary conditions in order to be solved. The annular domain has been reduced via the scaling to rectangular domain Ω, representing the unwrapped gap-averaged annulus. At each timestep it is necessary to specify suitable boundary conditions on $\partial\Omega$ in order to solve (25). We suppose that $\partial\Omega$ can be split into $\partial\Omega_\Psi$ and $\partial\Omega_S$:

$$\Psi = \Psi_b, \quad (\phi, \xi) \in \partial\Omega_\Psi, \tag{28}$$

$$\mathbf{S} \cdot \mathbf{n} = f, \quad (\phi, \xi) \in \partial\Omega_S, \tag{29}$$

where Ψ_b and f are specified boundary data. The conditions are explained below.

First, in the azimuthal direction if the geometry is fixed so that the narrow side of the annulus is the lowest side, then one may simplify the model by assuming that the flow is symmetric in ϕ along both wide and narrow sides:

$$\Psi(0, \xi, t) = 0, \tag{30}$$

$$\Psi(1, \xi, t) = 2Q(t), \tag{31}$$

where $Q(t)$ is the dimensionless flow rate (and $\Omega = [0, 1] \times [0, Z]$). Note that by rearranging (24), $\mathbf{S}$ can also be expressed in terms of the pressure gradients as

$$\mathbf{S} = \left(-r_a \frac{\partial \bar{p}}{\partial \xi} - \frac{r_a(\rho - 1)\cos\beta}{Fr^2}, \frac{\partial \bar{p}}{\partial \phi} - \frac{r_a(\rho - 1)\sin\beta \sin\pi\phi}{Fr^2} \right).$$

Thus, the symmetry condition $\bar{\bar{v}} = 0$, which gives $S_\xi = 0$, also implies that $\frac{\partial \bar{p}}{\partial \phi} = 0$.

On the other hand, suppose we consider a full annulus, with no symmetry imposed at wide and narrow sides ($\Omega = [0, 2] \times [0, Z]$). Then an alternate to (30) and (31) would be

$$\Psi(\phi + 2, \xi, t) = \Psi(\phi, \xi, t) + 4Q(t), \tag{32}$$

fixing only the total flow rate. In using (32), if one wanted to work with the pressure, the pressure would be 2-periodic in ϕ.

Secondly, for the end conditions, following [9], we might expect to impose Dirichlet conditions at the inflow, $\xi = 0$:

$$\Psi(\phi, 0, t) = \Psi_0(\phi, t), \tag{33}$$

e.g. a uniform inflow velocity can be specified, reflecting the fact of some kind of entry/development region, following local mixing as the fluids enter the annulus. Similarly, at the outflow ($\xi = Z$), it might be appropriate to assume a fully developed flow profile:

$$\Psi(\phi, Z, t) = \Psi_Z(\phi, t). \tag{34}$$

The fully developed profile above of course needs to be specified. The natural way to do this is by neglecting ξ-derivatives in (25), due to the length of the annulus, which leads to

$$\frac{\partial}{\partial \phi}[S_\phi + b_\phi] = 0,$$

which in turn implies that $\frac{\partial \bar{p}}{\partial \xi}$ is independent of ϕ. The fully developed profile would be found computationally by decreasing $\frac{\partial \bar{p}}{\partial \xi}$, which increases the axial velocity at each ϕ (hence the flowrate), until the net imposed flowrate through the exit section is attained. Although this appears a convoluted procedure, it is straightforward numerically.

As an alternative to (33) and (34), one might impose Neumann conditions ($\frac{\partial \Psi}{\partial \xi} = 0$) at each end of the annulus, e.g. as in [10]. Note that the Neumann condition, implies that $S_\xi = 0$, which specifies $\mathbf{S} \cdot \mathbf{n}$ on the boundary with outward normal $\mathbf{n}$, i.e. a condition of type (29). Depending on the density gradients at inflow and outflow we might choose to specify $\mathbf{S} \cdot \mathbf{n}$ in terms of the buoyancy $\mathbf{b} \cdot \mathbf{n}$.

3 Mass transport

We now turn to transport of the different fluids along the annulus, assuming that at each time the elliptic problem (25) can be solved to give the gap-averaged velocity field. This suggests a similar model reduction will be appropriate for the different fluids and now proceed to derive this.

The concentrations of each individual fluid component c_k are modelled by an advection–diffusion equation:

$$\frac{\partial c_k}{\partial \hat{t}} + \frac{1}{\hat{r}}\frac{\partial}{\partial \hat{r}}[\hat{r}\hat{u}c_k] + \frac{1}{\hat{r}}\frac{\partial}{\partial \theta}[\hat{v}c_k] + \frac{\partial}{\partial \hat{\xi}}[\hat{w}c_k] = \hat{\nabla} \cdot [\hat{D}_{k,m}\hat{\nabla}c_k], \tag{35}$$

where $\sum_{k=1}^{K} c_k = 1$ and $\hat{D}_{k,m}$ represents the molecular diffusivity of species k within the mixture. For the turbulent flow, we apply the usual Reynolds decomposition and introduce the closure:

$$-\overline{\hat{\mathbf{u}}' c_k'} = \hat{D}_t \hat{\nabla} \bar{c}_k, \tag{36}$$

where $\hat{D}_t$ is the turbulent diffusivity of species k (assumed the same for each species). Equation (35) becomes

$$\frac{\partial \bar{c}_k}{\partial \hat{t}} + \frac{1}{\hat{r}}\frac{\partial}{\partial \hat{r}}[\hat{r}\bar{\hat{u}}\bar{c}_k] + \frac{1}{\hat{r}}\frac{\partial}{\partial \theta}[\bar{\hat{v}}\bar{c}_k] + \frac{\partial}{\partial \hat{\xi}}\left[\bar{\hat{w}}\bar{c}_k\right] = \hat{\nabla} \cdot [(\hat{D}_t + \hat{D}_{k,m})\hat{\nabla}\bar{c}_k\Big]. \tag{37}$$

We now apply the scaling introduced earlier. We anticipate that the main diffusive term is $\hat{D}_t$ which will scale with the local gap width and friction velocity, but here introduce a global scale: $\delta_0 \hat{r}_{a,0} \hat{\bar{W}}$ for the purposes of simplification. The scaled system is

$$\frac{\delta_0}{\pi}\left(\frac{\partial \bar{c}_k}{\partial t} + \frac{\partial}{\partial y}[\bar{u}\bar{c}_k] + \frac{1}{r_a}\frac{\partial}{\partial \phi}[\bar{v}\bar{c}_k] + \frac{\partial}{\partial \xi}[\bar{w}\bar{c}_k]\right) = \frac{\partial}{\partial y}\left[D_k \frac{\partial \bar{c}_k}{\partial y}\right] + \left(\frac{\delta_0}{\pi}\right)^2 \nabla_{\mathbf{a}} \cdot [D_k \nabla_a \bar{c}_k] \tag{38}$$

with $D_k = D_t + 1/Pe_k$ and $Pe_k = \delta_0 \hat{r}_{a,0} \hat{\bar{W}} / \hat{D}_{k,m}$, $D_t = \hat{D}_t / [\delta_0 \hat{r}_{a,0} \hat{\bar{W}}]$. On the left-hand side of (38), we have neglected terms that come from approximating geometry/curvature effects, which are $O(\delta/\pi)$ smaller than those considered. On the right-hand side, we have also neglected terms of $O(\delta/\pi)$ that come from approximating the radial diffusion term.

Eliminating these curvature/geometry terms *only*, while retaining the other terms may appear questionable as a perturbation procedure. However, note that the intention is to include the leading-order effects of all physically relevant transport processes. It is evident that (38) represents a singular perturbation, in which the leading-order concentration will be constant across the annular gap (see below). We thus retain the first order advective component on the left-hand side as this is responsible both for advection of the mean concentration and dispersive effects, within the plane of the narrow annulus. We also wish to evaluate the balance between turbulent diffusion and dispersion within the (ϕ, ξ)-plane and consequently retain the diffusive terms in (ϕ, ξ) directions. Lastly, although curvature may effect cross-gap diffusion the leading-order effect is included in the order 1 terms.

3.1 Dispersion effects

We look for a perturbation approximation to (38) in terms of the parameter $\delta_0/\pi \ll 1$. The velocity is assumed to have the following form

$$\bar{\mathbf{u}} = \bar{\bar{\mathbf{u}}}_0 + \tilde{\mathbf{u}}_0 + \left(\frac{\delta_0}{\pi}\right)\tilde{\mathbf{u}}_1 + \left(\frac{\delta_0}{\pi}\right)^2 \tilde{\mathbf{u}}_2 + \cdots, \tag{39}$$

$$0 = \int_{-H}^{H} \tilde{\mathbf{u}}_j \,\mathrm{d}y, \quad j = 0, 1, 2\ldots, \tag{40}$$

i.e. the velocity (which we recall is anyway ensemble averaged) is decomposed into a gap-averaged component $\bar{\bar{\mathbf{u}}}_0$ and successive components at each order that describe the y-variation. We assume that $\bar{\bar{\mathbf{u}}}_0 = (0, \bar{\bar{v}}, \bar{\bar{w}})$, as defined in (18), and that $\tilde{u}_0 = 0$, i.e. the radial component of velocity only arises at the first order. Similarly we write

$$\bar{c}_k = \bar{c}_{k,0} + \left(\frac{\delta_0}{\pi}\right)\bar{c}_{k,1} + \left(\frac{\delta_0}{\pi}\right)^2 \bar{c}_{k,2} + \cdots, \tag{41}$$

$$0 = \int_{-H}^{H} \bar{c}_{k,j} \,\mathrm{d}y, \quad j = 1, 2\ldots, \tag{42}$$

Here following [39,40], we use method of multiple timescales suggested by [41] in which we assume that the variables respond on both the advective time t and on a slower timescale $T = (\delta_0/\pi)\, t$, where we expect diffusive effects to come into play. Note that no-slip boundary conditions are satisfied by $\bar{\mathbf{u}}$ at the walls, where also the diffusive fluxes of $\bar{c}_k$ are zero (Neumann condition).

Substituting these expressions into (38), we find that at leading-order $\bar{c}_{k,0}$ is independent of y, as we have already assumed previously in analysing the momentum balance. From (42) we interpret $\bar{c}_{k,0}$ as the gap-averaged mean concentration. The first-order equations are as follows:

$$\left(\frac{\partial \bar{c}_{k,0}}{\partial t} + \frac{\partial}{\partial y}[\tilde{u}_0 \bar{c}_{k,0}] + \nabla_a \cdot [\bar{c}_{k,0}(\bar{\bar{v}} + \tilde{v}_0, \bar{\bar{w}} + \tilde{w}_0)]\right) = \frac{\partial}{\partial y}\left[D_{k,0}\frac{\partial \bar{c}_{k,1}}{\partial y}\right]. \tag{43}$$

Integrating across the channel shows that

$$\frac{\partial \bar{c}_{k,0}}{\partial t} + (\bar{\bar{v}}, \bar{\bar{w}}) \cdot \nabla_a \bar{c}_{k,0} = 0 \tag{44}$$

and on substituting back into (43) and using the continuity equation

$$\frac{\partial}{\partial y}\left[D_{k,0}\frac{\partial \bar{c}_{k,1}}{\partial y}\right] = (\tilde{v}_0, \tilde{w}_0) \cdot \nabla_a \bar{c}_{k,0}, \quad \Rightarrow \quad \frac{\partial \bar{c}_{k,1}}{\partial y} = \frac{\nabla_a \bar{c}_{k,0} \cdot \left(\int_{-H}^{y} (\tilde{v}_0, \tilde{w}_0)\,\mathrm{d}y'\right)}{D_{k,0}}. \tag{45}$$

The expression (44) says that on the advective timescale t the leading-order concentration is simply advected along the streamlines.

To understand evolution on the slow timescale T, we move to a frame of reference moving along the gap-averaged streamlines. The coordinates (s, n) align locally with the directions $\mathbf{e}_s$ and $\mathbf{e}_n$: tangential and normal to the streamlines, respectively. The gap-averaged speed in the direction of the streamline is denoted $\bar{\bar{s}}_0 = \sqrt{\bar{\bar{v}}_0^2 + \bar{\bar{w}}_0^2} = |\nabla_a \Psi|/(2H)$. To further integrate (45), recall that in analysing the momentum balance in the previous section, we have shown that the leading-order turbulent velocity is in the direction of the pressure gradient. Therefore, the two vectors $(\bar{\bar{v}}_0, \bar{\bar{w}}_0)$ and $(\tilde{v}_0, \tilde{w}_0)$ are parallel and only in direction $\mathbf{e}_s$, i.e.

$$(\bar{\bar{v}}, \bar{\bar{w}}) \cdot \nabla_a \bar{c}_{k,0} = \bar{\bar{s}}_0 \frac{\partial \bar{c}_{k,0}}{\partial s} \quad \text{and} \quad (\tilde{v}_0, \tilde{w}_0) \cdot \nabla_a \bar{c}_{k,0} = \tilde{s}_0 \frac{\partial \bar{c}_{k,0}}{\partial s},$$

where $\tilde{s}_0(y)$ gives the variation in the mean speed across the narrow gap. Substituting into (43) and integrating the first order terms, we get

$$\bar{c}_{k,1} = \bar{c}_{k,1}(-H) + \frac{\partial \bar{c}_0}{\partial s} \int_{-H}^{y} \frac{1}{D_{k,0}} \int_{-H}^{y'} \tilde{s}_0 \; \mathrm{d}y'' \mathrm{d}y' = \bar{c}_{k,1}(-H) + \frac{\partial \bar{c}_0}{\partial s} k(y) \tag{46}$$

in which

$$k(y) = \int_{-H}^{y} \frac{1}{D_{k,0}} \int_{-H}^{y'} \tilde{s}_0 \; \mathrm{d}y'' \mathrm{d}y'.$$

By construction, $\bar{c}_{k,1}(-H) = -\bar{k} \frac{\partial \bar{c}_{k,0}}{\partial s}$ where $\bar{k}$ is the average of $k(y)$ across the gap. Thus, $\bar{c}_{k,1}$ is expressed in terms of $\frac{\partial \bar{c}_{k,0}}{\partial s}$ and the distribution of velocity across the gap. Before proceeding, note that the leading-order velocity is based on the narrow channel approximation, which leads to an even function: $\tilde{s}_0(y)$ is symmetric about $y = 0$. Also since

$$0 = \int_{-H}^{H} \tilde{s}_0(y) \; \mathrm{d}y = 2 \int_{0}^{H} \tilde{s}_0(y) \; \mathrm{d}y = 2 \int_{-H}^{0} \tilde{s}_0(y) \; \mathrm{d}y,$$

we may write

$$k(y) = \int_{-H}^{y} \frac{1}{D_{k,0}} \int_{0}^{y'} \tilde{s}_0 \; \mathrm{d}y'' \mathrm{d}y',$$

and note that the integral of $\tilde{s}_0(y)$ will be an odd function. The function $D_{k,0}(y)$ is also defined by the leading order velocity and can be assumed to be an even function. The integrand above is therefore also an odd function. From this, we may conclude that $k(y)$ is an even function and that $k(-H) = k(H) = 0$. Similarly, $\bar{c}_{k,1}$ is an even function of y.

At the next order of asymptotic expansion, in the moving frame of reference, we collect terms of $\mathcal{O}((\delta_0/\pi)^2)$:

$$\begin{aligned} \frac{\partial \bar{c}_{k,0}}{\partial T} &= -\nabla_a \cdot \left[\bar{c}_{k,1} (\tilde{v}_0, \tilde{w}_0) \right] + \nabla_{\mathbf{a}} . (D_{k,0} \nabla_a \bar{c}_{k,0}) \\ &\quad - \frac{\partial \bar{c}_{k,1}}{\partial t} - \bar{\bar{s}}_0 \frac{\partial \bar{c}_{k,1}}{\partial s} - \frac{\partial}{\partial y} (\tilde{u}_1 \bar{c}_{k,0}) - \nabla_a \cdot \left[\bar{c}_{k,0} (\tilde{v}_1, \tilde{w}_1) \right] \\ &\quad + \frac{\partial}{\partial y} \left(D_{k,0} \frac{\partial \bar{c}_{k,2}}{\partial y} \right) + \frac{\partial}{\partial y} \left(D_{k,1} \frac{\partial \bar{c}_{k,1}}{\partial y} \right) + \frac{\partial}{\partial y} \left(D_{k,2} \frac{\partial \bar{c}_{k,0}}{\partial y} \right). \end{aligned} \tag{47}$$

We integrate (47) across the gap width. The terms in the first line of (47) do not vanish. In the second line, the first two terms are linear in quantities that integrate to zero. For the last two terms, we use the incompressibility of $\tilde{\mathbf{u}}_1$:

$$\frac{\partial}{\partial y} (\tilde{u}_1 \bar{c}_{k,0}) + \nabla_a \cdot \left[\bar{c}_{k,0} (\tilde{v}_1, \tilde{w}_1) \right] = \tilde{\mathbf{u}}_1 \cdot \nabla \bar{c}_{k,0} = \nabla_a \bar{c}_{k,0} \cdot (\tilde{v}_1, \tilde{w}_1).$$

These terms now integrate to zero across the gap. In the third line, the terms vanish as there is no flux through the walls.

On substituting from (46), we see that the slow time evolution of $\bar{c}_{k,0}$ in the frame of reference moving along the streamline is governed by

$$2H\frac{\partial \bar{c}_{k,0}}{\partial T} = -\int_{-H}^{H}\frac{\partial}{\partial s}\left[\tilde{s}_0(k(y)-\bar{k})\frac{\partial \bar{c}_{k,0}}{\partial s}\right]\mathrm{d}y + \int_{-H}^{H}\nabla_{\mathbf{a}}.(D_{k,0}\nabla_a \bar{c}_{k,0})\,\mathrm{d}y. \tag{48}$$

The first term on the right-hand side of (48) is the Taylor dispersion term, which we write as follows:

$$\begin{aligned}\int_{-H}^{H}\frac{\partial}{\partial s}\left[\tilde{s}_0(k-\bar{k})\frac{\partial \bar{c}_{k,0}}{\partial s}\right]\mathrm{d}y &= \frac{\partial}{\partial s}\left[\left(\int_{-H}^{H}\tilde{s}_0 k\,\mathrm{d}y\right)\frac{\partial \bar{c}_{k,0}}{\partial s}\right] + 2\frac{\partial H}{\partial s}\frac{\partial \bar{c}_{k,0}}{\partial s}[\tilde{s}_0(H)\bar{k}]\\ &= -\frac{\partial}{\partial s}\left[2HD_T\frac{\partial \bar{c}_{k,0}}{\partial s}\right] + 2\frac{\partial H}{\partial s}\frac{\partial \bar{c}_{k,0}}{\partial s}[\tilde{s}_0(H)\bar{k}],\\ D_T &= \frac{1}{2H}\int_{-H}^{H}\frac{1}{D_{k,0}(y)}\left(\int_{-H}^{y}\tilde{s}_0(y')\mathrm{d}y'\right)^2\mathrm{d}y.\end{aligned}$$

The second term on the right-hand side of (48) reflects the average effect of the diffusivity $D_{k,0}$. At $y=\pm H$, the turbulent term vanishes, leaving only a negligible molecular contribution $1/Pe \ll 1$. Therefore, we can write

$$\begin{aligned}\int_{-H}^{H}\nabla_{\mathbf{a}}\cdot(D_{k,0}\nabla_a\bar{c}_{k,0})\,\mathrm{d}y &= \nabla_{\mathbf{a}}\cdot\int_{-H}^{H}(D_{k,0}\nabla_a\bar{c}_{k,0})\,\mathrm{d}y\\ &\quad -\nabla_a H\cdot\nabla_a\bar{c}_{k,0}[D_{k,0}(H)+D_{k,0}(-H)]\\ &= \nabla_{\mathbf{a}}\cdot[2H\bar{D}\nabla_a\bar{c}_{k,0}] + O(1/Pe),\\ \bar{D} &= \frac{1}{2H}\int_{-H}^{H}D_{k,0}\,\mathrm{d}y.\end{aligned}$$

Combining the above expressions with (44), reverting back to the single timescale t and transforming back into the fixed frame of reference, we arrive at the following equation for the evolution of the leading-order concentration:

$$\begin{aligned}\frac{\partial c_{k,0}}{\partial t} &= -(\bar{\bar{v}}_0,\bar{\bar{w}}_0)\cdot\nabla_a c_{k,0} + \frac{\delta_0}{\pi}\left(\frac{1}{2H}\mathbf{e}_s\cdot\nabla_a\left[(2HD_T)\mathbf{e}_s\cdot\nabla_a c_{k,0}\right]\right.\\ &\quad\left. -\frac{\bar{k}\tilde{s}_0(H)}{H}(\mathbf{e}_s\cdot\nabla_a H)(\mathbf{e}_s\cdot\nabla_a c_{k,0}) + \frac{1}{2H}\nabla_{\mathbf{a}}\cdot\left[2H\bar{D}\nabla_a\bar{c}_{k,0}\right]\right).\end{aligned}\tag{49}$$

Equation (49) describes how the leading-order concentrations of fluid k change. The right-hand side has four terms. Firstly, we have advection with the mean flow. Secondly, we have a pure Taylor-dispersion term, which we can see takes the form of an anisotropic diffusivity, i.e. only along the streamlines (in direction $\mathbf{e}_s$). The third term results from variations in width of the annulus. The fourth term on the right-hand side gives the averaged effect of the diffusivity. In [35], we have modelled the velocity profiles for the flow along a uniform plane channel, i.e. $\bar{\bar{s}}_0+\tilde{s}_0(y)$ and have used this, together with estimates of the turbulent diffusivity, to compute the Taylor dispersivity D_T. In general, it is found that $\bar{D} \ll D_T$. In highly turbulent flows, D_T decreases, but still remains two orders of magnitude larger than $\bar{D}$. Thus, it is the first two dispersive terms that are of most interest.

We may extract the variation of H from the first term and rewrite (49) as

$$\begin{aligned}\frac{\partial c_{k,0}}{\partial t} &= -(\bar{\bar{v}}_0,\bar{\bar{w}}_0)\cdot\nabla_a c_{k,0} + \frac{\delta_0}{\pi}\left(\mathbf{e}_s\cdot\nabla_a[D_T\mathbf{e}_s\cdot\nabla_a c_{k,0}] + \frac{1}{2H}\nabla_{\mathbf{a}}\cdot[2H\bar{D}\nabla_a\bar{c}_{k,0}]\right)\\ &\quad + \frac{\delta_0}{\pi}(\mathbf{e}_s\cdot\nabla_a H)(\mathbf{e}_s\cdot\nabla_a c_{k,0})\frac{D_T-D_T^*}{H},\end{aligned}\tag{50}$$

where

$$D_T^* = \bar{k}\tilde{s}_0(H) = -\frac{\tilde{s}_0(H)}{2H}\int_{-H}^{H}\frac{y}{D_{k,0}(y)}\int_{-H}^{y}\tilde{s}_0(y')\mathrm{d}y'\mathrm{d}y. \tag{51}$$

We see that nominally D_T^* has the same size as D_T. Note that the last term in (50) will vanish when the annulus is concentric. Also we should note that in most displacement flows through long annuli the streamlines are pseudo-parallel to the ξ-axis for most of the annulus and H generally varies slowly with ξ, so this last term is mostly insignificant. However, in *interfacial* regions between two displacing fluids we often see azimuthal velocities of a similar size to the axial velocity. These regions are of course also where the main Taylor dispersion term is active. Therefore, the interplay between these two terms needs investigating. Local closure expressions for D_T, D_T^* and $\bar{D}$, in terms of the expressions derived in [35], are given later in Appendix A.5.

3.2 Boundary conditions

Boundary conditions for (50) are generally that $c_{k,0}$ is specified at the inflow to the annulus, either from a pump schedule or from coupling with a predictive model of the downwards displacement flow in the casing. Along the sides of the annulus, either a symmetry condition is imposed, i.e. $\frac{\partial c_{k,0}}{\partial \phi} = 0$, or potentially a periodicity condition in the case that the full annulus is resolved and no symmetry is assumed. At the outflow, we generally assume that $\frac{\partial c_{k,0}}{\partial \xi} = 0$, although in cases of large density differences we may have counter-current flows with denser fluids entering the annulus and need to specify accordingly.

4 Annular displacement flow model

To summarize the derivations of the previous 2 sections, leading-order annular displacement flows (across mixed flow regimes) are governed by the coupled system:

$$\nabla_a \cdot [\mathbf{S} + \mathbf{b}] = 0 \tag{52}$$

$$\frac{1}{2H}\nabla_a \Psi = (\bar{\bar{w}}_0, -\bar{\bar{v}}_0), \tag{53}$$

$$\begin{aligned}\frac{\partial c_{k,0}}{\partial t} + (\bar{\bar{v}}_0, \bar{\bar{w}}_0)\cdot\nabla_a c_{k,0} = {} & \frac{\delta_0}{\pi}\left(\mathbf{e}_s\cdot\nabla_a\left[D_T\mathbf{e}_s\cdot\nabla_a c_{k,0}\right] + \frac{1}{2H}\nabla_{\mathbf{a}}\cdot\left[2H\bar{D}\nabla_a\bar{c}_{k,0}\right]\right)\\ & + \frac{\delta_0}{\pi}\left(\mathbf{e}_s\cdot\nabla_a H\right)\left(\mathbf{e}_s\cdot\nabla_a c_{k,0}\right)\frac{D_T - D_T^*}{H}\end{aligned} \tag{54}$$

with associated boundary conditions. Due to the lengthy derivation, we shall defer full analysis of this system to be future paper. Here we focus on presenting some example simulations that indicate the process complexity (Sect. 4.2) and give some basic estimates for diffusion/dispersion effects.

4.1 Computational overview

For brevity, we do not present algorithmic details here, as the method is very similar to that used in [7]. The computational domain is rectangular, and we use a second-order finite difference method on a staggered mesh: representing the fluid concentrations at cell centres and the stream function at the gridpoints (corners). We have used 30 mesh cells in the azimuthal direction and 100 cells along the annulus. At each timestep, the stream function is found by solving (52) using an augmented Lagrangian procedure as in [7]. This algorithm is slow to converge and not motivated by (or needed for) the turbulent regime, i.e. many faster methods could be employed. However, mixed flow regimes are common in primary cementing, and this algorithm resolves those parts of the flow where fluids are immobile due to the yield stress. Hence, we retain this feature at the expense of speed.

The concentration enters the stream function equation through the buoyancy field **b** and through the local fluid properties. Having found the stream, we construct the velocity field from (53) and advance the fluid concentrations in time by solving (54). The algorithm employed for the advective parts of (54) is the FCT scheme, as in [7], with the diffusive and dispersive terms discretized explicitly using central differences. For the non-diffusive problem, a concentric annulus with positive density difference leads to an analytical solution for the interface shape [9], which has been used as a validation problem.

4.2 Example displacement scenarios

To explain different features of our model, here we present a few displacement examples. We focus these examples at annulus dimensions that are more typical of a laboratory flow loop setting, with $\hat{r}_i = 6.5$ cm, $\hat{r}_o = 9$ cm, $\hat{Z} = 20$ m. The annulus will here be assumed vertical $\beta = 0$. More realistic well dimensions are saved for our later study in which we systematically explore turbulent and mixed regime effects. For all the results presented, we have restricted the simulation to only one half of the annulus—assuming symmetry at the wide and narrow sides.

Example 1 In the first example, we probe the effect of dispersion. Fluid 1 has properties: $\hat{\rho}_1 = 1100$ kg/m^3, $\hat{\kappa}_1 = 0.002$ Pa.s^n, $n_1 = 0.9$, $\hat{\tau}_{Y,1} = 0$ Pa. The displacing fluid has identical properties. The annulus has eccentricity $e = 0.5$ but is otherwise uniform, and the flow rate is constant ($Q = 0.01$ m^3/s). In this scenario as the fluids are identical, we expect a stream function that varies only with ϕ (parallel streamlines), i.e. the flow is fully developed and velocity is only in the axial direction. Figure. 2 presents a colourmap of the fluid concentrations as they advance along the annulus: fluid 1 (red) is displaced by fluid 2 (blue). The eccentricity leads to faster flows on the wider side (W) than on the narrow side (N). The interface constantly elongates as a consequence. In Fig. 2a, we have set to zero all terms on the right-hand side of (54). In Fig. 2b, we included Taylor dispersion and the turbulent diffusivity (first and second terms on the right-hand side of (54). Finally, Fig. 2c solves (54) in its complete form.

Figure 2a essentially shows the performance of the FCT scheme in advecting the front. Numerical smearing (diffusion/dispersion) of the front is present but is kept to a few cells in width. For this flow in particular (1D), there are no secondary flows that can advectively mix intermediate concentrations. The front is sharpened by mesh refinement of course, at the expense of longer computational times. As commented and illustrated in Fig. 6, turbulent diffusivity is at least two orders of magnitude smaller than Taylor dispersion. Including the diffusivity terms here has little effect as shown in Fig. 2a; numerical diffusion/dispersion has a larger effect on these mesh sizes.

Figure 2b shows a significant effect of D_T, in comparison to Fig. 2a. The front spreads most on the wide side, thickening to about 2 m by the end of the annulus. We observe that there is no discernible difference between Figs. 2b, c, although the term D_T^* is in fact larger than D_T (see Fig. 6). This illustrates the points made earlier regarding the last term in (54). Here the streamlines are parallel, so $\mathbf{e}_s \cdot \nabla_a c_{k,0}$ is only in the ξ direction. Equally, H does not vary with ξ so that $\mathbf{e}_s \cdot \nabla_a H = 0$.

Example 2 Our second example explores mixed flow regimes and buoyancy effects, again in an eccentric annulus ($e = 0.5$). In Fig. 3, fluid 1 (red) has properties: $\hat{\rho}_1 = 1300$ kg/m^3, $\hat{\kappa}_1 = 0.002$ Pa.s^n, $n_1 = 0.8$, $\hat{\tau}_{Y,1} = 0$ Pa, and fluid 2 (blue) has properties: $\hat{\rho}_2 = 1200$ kg/m^3, $\hat{\kappa}_2 = 0.004$ Pa.s^n, $n_1 = 0.9$, $\hat{\tau}_{Y,1} = 1$ Pa. The fluids are pumped at $Q = 0.01$ m^3/s. The fluid rheologies are not very different to example 1, but there is a significant (unstable) density difference. Figure 3a is an extreme example of an unsteady displacement. There is an unfavourable density difference but favourable rheology difference between the displaced and displacing fluids. However, this rheology difference is apparently ineffective as we observe that fluid two rapidly channels up the wide side of the annulus by-passing fluid 1. The flow regimes are shown in the last two panels of the figure, at 2 times late in the displacement (white,

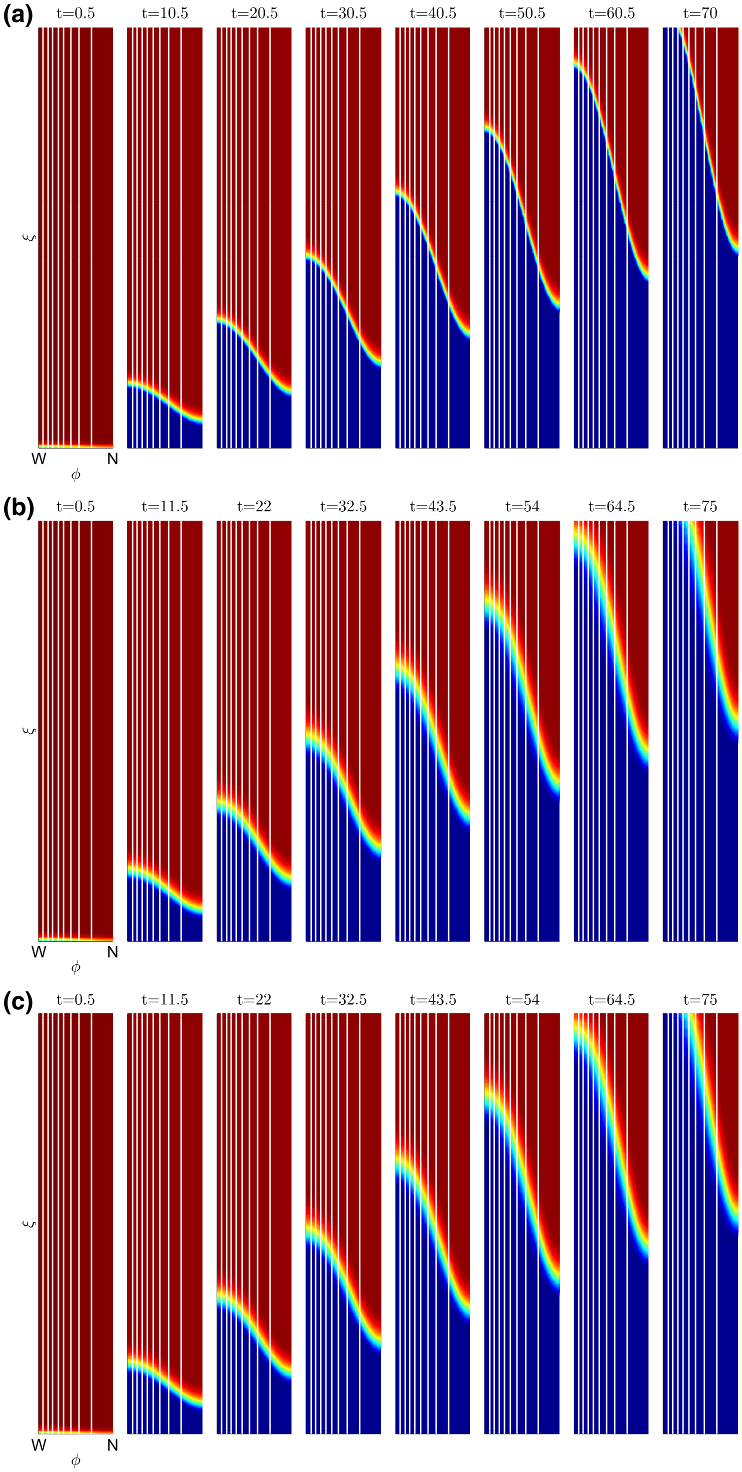

Fig. 2 Turbulent displacement in an eccentric annulus: $e = 0.5$. *Colour maps* of the concentration are shown in dimensionless coordinate system (ϕ, ξ) at different dimensionless times as the front progresses along the annulus. *White lines* are streamlines with spacing $\Delta\Psi = 0.25$. **a** No dispersion or diffusivity ($\bar{D} = D_T = D_T^* = 0$); **b** only Taylor dispersion ($D_T^* = D_T$); **c** both dispersive terms included. Fluid 1 (*red*) properties: $\hat{\rho}_1 = 1100$ kg/m^3, $\hat{\kappa}_1 = 0.002$ Pa.s^n, $n_1 = 0.9$, $\hat{\tau}_{Y,1} = 0$ Pa; fluid 2 is identical (*blue*). (Color figure online)

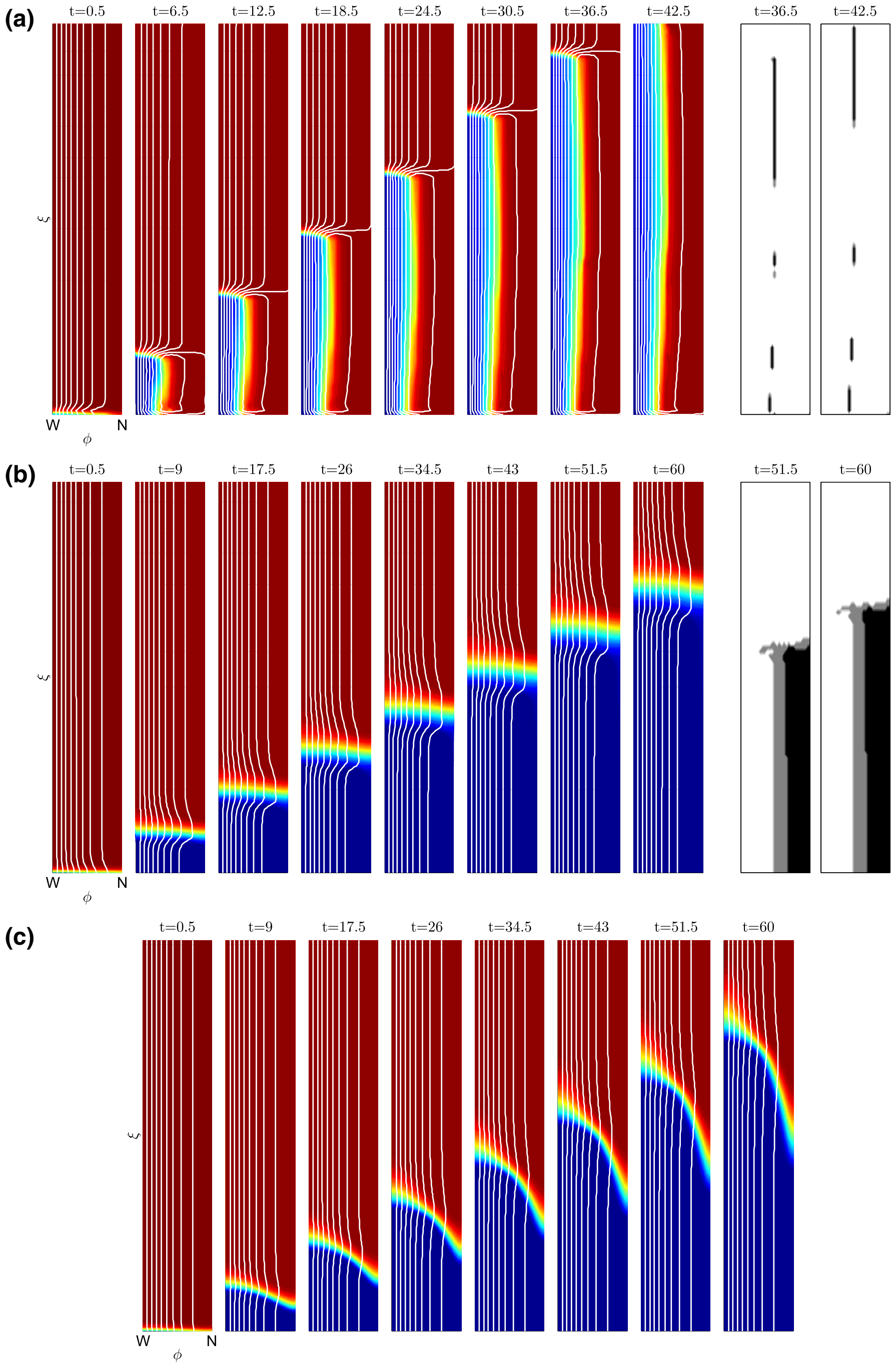

Fig. 3 **a**, **b** Mixed regime displacement flows in an eccentric annulus $e = 0.5$ at $\hat{Q}$ =0.01 m^3/s. *White lines* are streamlines with $\Delta\Psi = 0.25$. The last 2 panels on the right show the flow regime: *white*, *grey* and *black* regions are turbulent, transitional and laminar, respectively. **a** Unsteady displacement with properties: fluid 1 (*red*), $\hat{\rho}_1 = 1300$ kg/m^2, $\hat{\kappa}_1 = 0.002$ Pa.s^n, $n_1 = 0.8$, $\hat{\tau}_{Y,1} = 0$ Pa; and fluid 2 (*blue*), $\hat{\rho}_2 = 1200$ kg/m^3, $\hat{\kappa}_2 = 0.004$ Pa.s^n, $n_2 = 0.9$, $\hat{\tau}_{Y,2} = 1$ Pa. **b** Steady displacement with properties: fluid 1 (*red*), $\hat{\rho}_1 = 1100$ kg/m^3, $\hat{\kappa}_1 = 0.002$ Pa.s^n, $n_1 = 0.9$, $\hat{\tau}_{Y,1} = 0$ Pa; and fluid 2 (*blue*), $\hat{\rho}_2 = 1300$ kg/m^3, $\hat{\kappa}_2 = 0.01$ Pa.s^n, $n_1 = 0.7$, $\hat{\tau}_{Y,1} = 1$ Pa. **c** A fully turbulent unsteady displacement with the same fluids as case b, but now $\hat{Q}$ = 0.05 m^3/s. (Color figure online)

grey and black regions are turbulent, transitional and laminar, respectively). We observe ahead of the front that fluid 1 is turbulent all around the annulus. Primarily turbulent flows are found behind the front (in both fluids). This strange flow configuration results because fluid 1 is in fact flowing backwards against the displacement direction, on the narrow side behind the displacement front.

The second row of this example shows another mixed regime displacement. The fluid rheologies are only slightly changed from Fig. 3a, but the density difference is reversed, i.e. fluid 2 is heavier than fluid 1. We see a displacement front that is approximately steady (apart from dispersion at the interface) and which effectively removes fluid 1 from the annulus. This reinforces the impression that the rheological difference between the two fluids is largely irrelevant: the steady displacement results from the stabilizing density difference, whereas that in Fig. 3a was unsteady. In this example, mixed regime flows are found behind the advancing displacement front. Due to the eccentricity and the yield stress in fluid 2, the flow ranges from fully turbulent through transitional to a laminar regime as we move azimuthally.

Figure 3a, b gives the impression that in turbulent displacements, buoyancy effects play a key role. This runs slightly counter to the intuitive notion that turbulent flows are effective in spreading momentum azimuthally. To explore this, we further increase the flow rate to $\hat{Q} = 0.05$ m^3/s in Fig. 3c, keeping the fluid properties the same as in b. Remarkably, the more turbulent flow appears to displace less effectively. We observe that the front advances and elongates along the wide side of the annulus. The concentration profiles are similar to those of Example 1.

Intuitively what has happened here is that the turbulent stresses have increased (approximately quadratically) with the increasing flow rate and now dominate the stabilizing buoyancy terms. At this point, neither buoyancy nor rheology is relevant in comparison to the turbulent stresses. In this highly turbulent limit, the asymptotic growth of τ_w (see Fig. 5a) is largely independent of n. Thus, we expect a similar distribution of velocity around the annulus in both fluids and observe that the frontal evolution is primarily advective and unidirectional.

Example 3 In our final example, we explore the effects of dispersion in a more complex displacement scenario. Here fluid 1 (red) is displaced by sequentially pumping fluid 2 (green) and then fluid 3 (blue), with properties: $\hat{\rho}_1 = 1300$ kg/m^3, $\hat{\kappa}_1 = 0.002$ Pa.s^n, $n_1 = 0.8$, $\hat{\tau}_{Y,1} = 0$ Pa; $\hat{\rho}_2 = 1100$ kg/m^3, $\hat{\kappa}_2 = 0.05$ Pa.s^n, $n_2 = 1$, $\hat{\tau}_{Y,2} = 1$ Pa; $\hat{\rho}_3 = 1300$ kg/m^3, $\hat{\kappa}_3 = 0.002$ Pa.s^n, $n_3 = 0.8$, $\hat{\tau}_{Y,3} = 0$ Pa. Thus, the unstable density difference is expected to destabilize the front between fluids 1 and 2, whereas the stable density difference between fluids 2 and 3 is expected to stabilize the front between fluids 2 and 3. The annulus is now concentric.

Figure 4a shows that what we expect does take place. The flows are turbulent and since the annulus is concentric we might hope for a steady uniform front to advance. The density difference between fluids 1 and 2 however promotes instability. Note that the system is mathematically analogous to a 2D miscible porous media displacement, with a nonlinear flow law. We expect the adverse density gradient to be vulnerable to fingering-type instabilities at the diffuse front, and once these start asymmetries will grow as we observe. Indeed, the initial instability grows and we see that the unstable fluid 2 eventually advects ahead of fluid 3, i.e. as a large buoyant droplet. Presumably, if the annulus was mildly eccentric this would influence the azimuthal position where the instabilities first arise and how they develop. The second interface has no fingering instability between fluids 2 and 3 and due to the positive buoyancy is stabilizing.

As Fig. 3c suggests, here we might expect that if we increase flow rate, then the flow loses its sensitivity to density difference and the interface between fluids 1 and 2 may become stable. In Fig. 4b, we test this idea. We increase the flow rate to $Q = 0.05\,$m^3/s and observe that this stabilizes the interface between fluids 1 and 2 in spite of their unsteady density difference. Unlike example 2, the annulus is now concentric so that the geometry does not itself have any bias, and we appear to have a steady (but dispersive) displacement.

4.3 Estimates of diffusion/dispersion in turbulent displacements

The example simulations of the previous section reveal some interesting physical features that we may now understand better via an order of magnitude analysis. Firstly, having determined that the advective contributions to Taylor

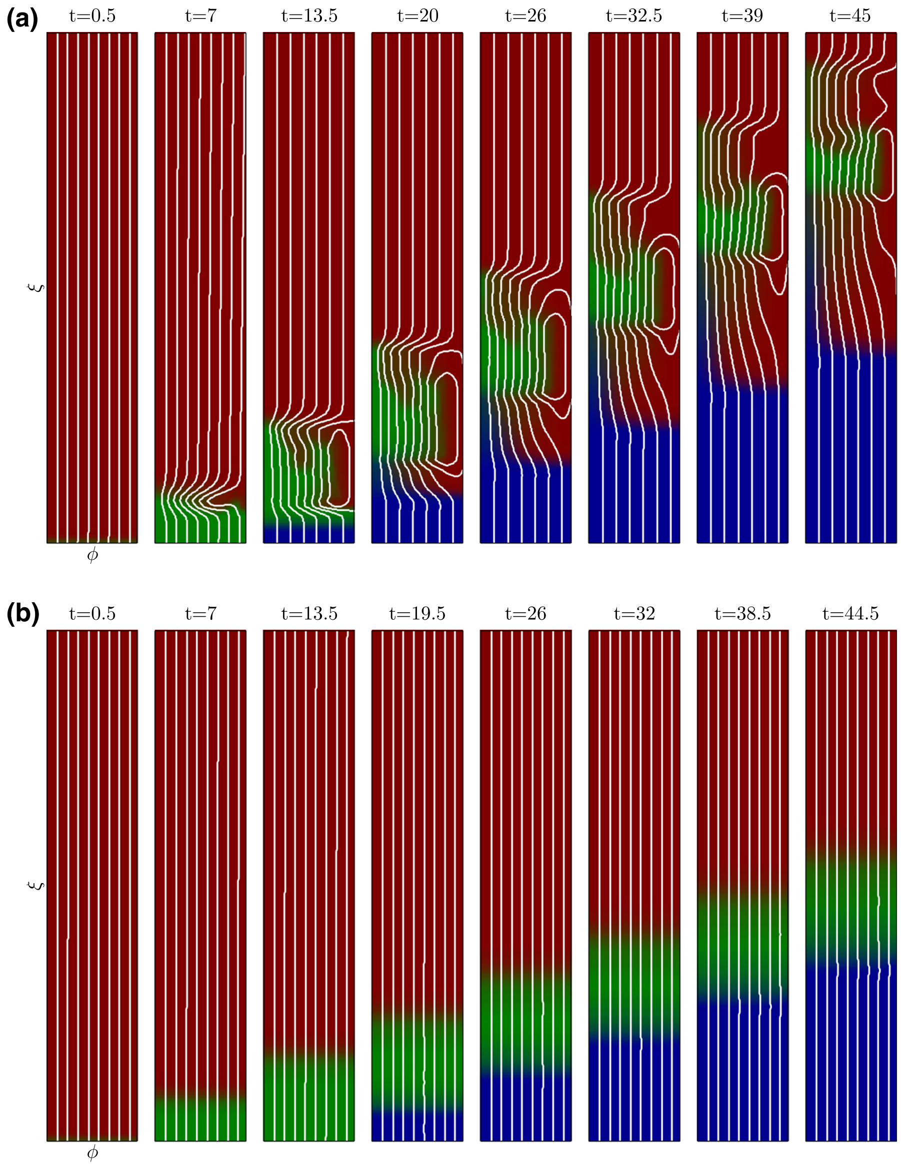

Fig. 4 Turbulent displacement in a *concentric* annulus with 3 fluids. *White lines* are streamlines with spacing $\Delta\Psi = 0.25$. Fluid 1 (*red*): $\hat{\rho}_1 = 1300\ \mathrm{kg/m^3}$, $\hat{\kappa}_1 = 0.002\ \mathrm{Pa.s}^n$, $n_1 = 0.8$, $\hat{\tau}_{Y,1} = 0$ Pa; fluid 2(*green*): $\hat{\rho}_2 = 1100\ \mathrm{kg/m^3}$, $\hat{\kappa}_2 = 0.05\ \mathrm{Pa.s}^n$, $n_2 = 1$, $\hat{\tau}_{Y,2} = 1$ Pa; fluid 3 (*blue*): $\hat{\rho}_3 = 1300\ \mathrm{kg/m^3}$, $\hat{\kappa}_3 = 0.002\ \mathrm{Pa.s}^n$, $n_3 = 0.8$, $\hat{\tau}_{Y,3} = 0$ Pa. **a** $Q = 0.01\ \mathrm{m^3/s}$; **b** $Q = 0.05\ \mathrm{m^3/s}$. (Color figure online)

dispersion have little effect in regular annuli, we can focus on the first and second terms on the right-hand side of (54), i.e. Taylor dispersion and mean turbulent diffusivity. Regarding the mean turbulent diffusivity, a rudimentary analysis suggests that the turbulent diffusivity scales with the gap width times the friction velocity, which in our variables corresponds to

$$\hat{\hat{D}} \sim \hat{W}_0 = \delta_0 \sqrt{f_f}\, \hat{r}_{a,0} \hat{\hat{W}} |\nabla_a \Psi|, \tag{55}$$

where f_f is the friction factor (see Sect. 1). Thus, the time to diffuse across the annular gap is approximately

$$\hat{t}_{\text{gap}} \sim \frac{[H\delta_0\hat{r}_{a,0}]^2}{\hat{\hat{D}}} \sim \frac{\delta_0\hat{r}_{a,0}2H}{\sqrt{f_f}\hat{\hat{W}}(|\nabla_a\Psi|/2H)}.$$

Physically, this is at most a few seconds in any turbulent section of a typical cemented annulus, which is of course why the Taylor dispersion regime is always relevant. Note though that (55) is only applicable to turbulent parts of the annulus. Secondly, note that as $\delta_0/\pi \rightarrow 0$, $\hat{t}_{gap} \rightarrow 0$ and thus formally, in the limit of our narrow-gap model, this mixing is effectively infinite.

Secondly, we have seen that in many situations displacement fronts tend to elongate as the displacement proceeds. Thus, we may ask instead how long it takes for turbulent diffusivity to diffuse azimuthally:

$$\hat{t}_{\text{azimuth}} \sim \frac{[\pi\hat{r}_{a,0}]^2}{\hat{\hat{D}}} \sim \frac{\pi^2\hat{r}_{a,0}}{\delta_0\sqrt{f_f}\hat{\hat{W}}}.$$

Evidently $\hat{t}_{\text{azimuth}} \rightarrow \infty$ as $\delta_0/\pi \rightarrow 0$. More generally this estimate could take many hundreds of seconds in a cemented well. Whether this is relevant depends on the time taken to cement a well segment of length $\hat{Z}$, $\hat{t}_{\text{cem}} = \hat{Z}/\hat{\hat{W}}$. Therefore, azimuthal mixing takes place approximately when $\hat{Z}/\hat{\hat{W}} \gtrsim \hat{t}_{\text{azimuth}}$, i.e.

$$\frac{\pi^2\hat{r}_{a,0}}{\delta_0\sqrt{f_f}\hat{Z}} \lesssim 1.$$

Lengths of several hundred metres are required for equality above and we conclude that azimuthal turbulent diffusion is only likely to occur in long cemented sections. The fraction of the azimuthal distance over which turbulent diffusivity spreads across the interface is roughly

$$\frac{\sqrt{\hat{\hat{D}}\hat{Z}/\hat{\hat{W}}}}{\pi\hat{r}_{a,0}} = \sqrt{\frac{\delta_0\sqrt{f_f}\hat{Z}}{\pi^2\hat{r}_{a,0}}}.$$

It seems that the direct effects of turbulent diffusivity may be significant in long wells, in diffusing the front azimuthally. However, such conclusions are premature and require a more extensive study. Note, for e.g., that the estimates made above are really based on a model scenario in which 2 parallel streams of fluid enter the annulus axially and diffuse azimuthally. Instead displacement flows are dynamic and additional timescales enter this type of estimate, e.g. the development time of the front, in order to elongate, and the axial extent of the elongated interface.

In the streamwise direction, as we have seen, Taylor dispersion will dominate. In dimensional terms, the Taylor dispersivity gives a streamwise diffusivity of size: $\delta_0\hat{\hat{W}}\hat{r}_{a,0}D_T$, with D_T of order 1. We see that after a time $\hat{Z}/\hat{\hat{W}}$ Taylor dispersion has typically spread the displacement front a distance $\sqrt{\delta_0\hat{Z}\hat{r}_{a,0}D_T}$, which is typically in the range of $1-20$ m. Again, such estimates are crude and rely on the streamlines being pseudo-parallel to the annulus axis. Situations such as the steady displacement of Fig. 3b require better understanding, as a steady displacement in an eccentric annulus implies that the streamlines are not axial in the vicinity of the displacement front.

5 Conclusions

In this paper, we have derived a practical leading-order model for simulating 2D turbulent and mixed regime displacement flows, as encountered in the process of primary cementing. The model presented complements that derived in [6] which was focused at laminar displacement flows. Indeed this model is included in that developed here, as the description for laminar displacements. However, the leading-order turbulent model has two main differences with [6].

First, the treatment of the momentum equations differs. Unlike the laminar flow, the turbulent Reynolds stress components all have similar size. The leading-order flow is a turbulent shear flow, but only due to differential scaling of the lengths. At the next order of approximation many more unknowns enter the model. Having derived the turbulent shear flow the analysis is similar to [6] in developing the field equations for the stream function (or pressure), but with the closure expressions coming from turbulent-flow hydraulics.

The second principal difference comes in the treatment of the fluid concentrations. First we note that the assumed decoupling of averaged concentration from velocity, in the advective part of (54), is more valid here than for the laminar model in [6]. Second, following our analysis, we find that turbulent flows are governed by complex diffusive and dispersive transport processes (absent in the laminar flows). The largest effect is Taylor dispersion, which diffuses only along the streamlines. The gap-averaged turbulent diffusivity acts isotropically but appears to be relevant only in sufficiently long wells. We have also derived terms that describe the influence of annulus gap variations on dispersion, again in the streamwise direction. These terms collectively are complex to understand, and in this paper, we have restricted ourselves to a few sample computations. For the laminar displacement flow, only molecular diffusion should be present, which results in smaller effects than those here.

The examples presented show only a few (of many) interesting effects, based on simulations of displacement flows along a small lab-scale annulus. As expected, rheology plays only a minor role in these turbulent flows, but density differences remain vitally important it appears. We have observed both steady and unsteady displacements (i.e. those in which the front elongates along the annulus), similar to in laminar displacements, but now with diffuse frontal regions. However, although phenomenologically similar the underlying physical conditions under which these flows arise are not yet studied or understood. This paper has primarily focused on developing the modelling tools, and our future research will be directed towards analysing these flows in depth.

Acknowledgements This research has been carried out at the University of British Columbia, supported financially by the British Columbia Oil and Gas Commission, by BC OGRIS, and partly by NSERC and Schlumberger through CRD Project 444985-12.

Appendix A: The wall shear stress closure

Here we outline the closure relationship that defines the dimensionless $\tau_w(|\nabla_a \Psi|; \phi, \xi, t)$, locally in the annulus, and hence

$$\mathbf{S} = \frac{r_a \tau_w(|\nabla_a \Psi|)}{H|\nabla_a \Psi|} \nabla_a \Psi.$$

we follow the methods in [35], where the flow of a Herschel–Bulkley fluid along a narrow channel is studied in laminar, transitional, and turbulent regimes.

We start by reconstructing the dimensional variables, which are then scaled following [35]. Given the shear stress scale $\hat{\tau}_0$, the dimensional wall shear stress is $\hat{\tau}_w = \hat{\tau}_0 \tau_w$. The dimensional mean speed (averaged across the local gap) and the dimensional local annular gap are given as

$$\hat{W}_0 = \hat{\hat{W}} \frac{1}{2H} |\nabla_a \Psi|, \qquad 2\hat{H} = 2H\delta_0 \hat{r}_{a,0} \tag{56}$$

recall that $\hat{\hat{W}}$ is the velocity scale for the entire annulus. We also assume that, according to the concentrations of the fluids at (ϕ, ξ, t), we may construct the dimensional local mixture density $\hat{\rho}$ and the rheological parameters $\hat{\tau}_Y, \hat{\kappa}, n$.

Now, following [35], we define

$$\hat{\dot{\gamma}}_N = \frac{6\hat{W}_0}{2\hat{H}}, \qquad \hat{\kappa}_p = \hat{\kappa} \left(\frac{2n+1}{3n} \right)^n . \tag{57}$$

The power-law Reynolds number is

$$Re_p = \frac{6\hat{\rho}\hat{W}_0^2}{\hat{\kappa}_p(\hat{\dot{\gamma}}_N)^n}. \tag{58}$$

The Hedström number and scaled wall shear stress are

$$He = \hat{\tau}_Y \left(\frac{\hat{\rho}^n(2\hat{H})^{2n}}{\hat{\kappa}_p^2}\right)^{1/(2-n)}, \quad H_w = \hat{\tau}_w \left(\frac{\hat{\rho}^n(2\hat{H})^{2n}}{\hat{\kappa}_p^2}\right)^{1/(2-n)}. \tag{59}$$

The procedure in [35] gives a detailed description of the mapping from Re_p to H_w and vice versa, which is parameterized by (n, He). Observe that $H_w \propto \tau_w$ and $Re_p \propto |\nabla_a \Psi|^{2-n}$, so the mapping $H_w \leftrightarrow Re_p$ defines our closure relation. Figure 5 shows an example of this mapping for different n at $He = 100$. The sensitivity to He is not extreme. We now outline the methodology in the different regimes.

A. 1 Laminar flows

For laminar regime the mapping $H_w \leftrightarrow Re_p$ (i.e. $\hat{\tau_w} \leftrightarrow \hat{W}_0$) is

$$\frac{(6Re_p)^{n/(2-n)}}{H_w} = E\left(n, \frac{He}{H_w}\right), \tag{60}$$

where

$$E(n, y_Y) = (1 - y_Y)^{(n+1)}\left(\frac{n}{n+1}y_Y + 1\right)^n, \tag{61}$$

i.e. $y_Y = He/H_w = \tau_Y/\tau_w$, which is the dimensionless width of the plug region. This nonlinear relationship is resolved to give $H_w(Re_p)$ and hence to define $\mathbf{S}$.

It is noted that $\mathbf{S}/|\nabla_a \Psi|$ is singular as $|\nabla_a \Psi| \to 0$, which is the limit where the yield stress of the fluid is not exceeded at the walls of the channel and $\tau_w < \tau_Y$ is indeterminate. In the laminar displacement model of [6,7], the vector $\mathbf{S}$ is defined explicitly to reflect this yielding phenomenon:

$$\mathbf{S} = \left[\frac{r_a \chi(|\nabla_a \Psi|)}{|\nabla_a \Psi|} + \frac{r_a \tau_Y}{H|\nabla_a \Psi|}\right]\nabla_a \Psi \quad \Leftrightarrow \quad |\mathbf{S}| > \frac{r_a \tau_Y}{H}, \tag{62}$$

$$|\nabla_a \Psi| = 0 \quad \Leftrightarrow \quad |\mathbf{S}| \le \frac{r_a \tau_Y}{H}. \tag{63}$$

To connect the model derivation here with that of [6,7], note that the function $\chi(|\nabla_a \Psi|)$ is simply

$$\chi(|\nabla_a \Psi|) = \frac{\tau_w(|\nabla_a \Psi|) - \tau_Y}{H}, \tag{64}$$

where τ_w is defined implicitly from (60).

The function $\chi(|\nabla_a \Psi|)$ increases strictly monotonically (as does $\tau_w(|\nabla_a \Psi|)$). We can examine the limits of (60), both as $H_w \to \infty$ and as $H_w \to He$ (yield limit). For the latter, we find

$$Re_p^{n/(2-n)} \sim [H_w - He]^{n+1} \quad \Rightarrow \quad \chi \sim |\nabla_a \Psi|^{n/(n+1)};$$

see Fig. 5b. As $H_w \to \infty$, we find $Re_p^{n/(2-n)} \sim H_w$, i.e. $\chi \sim |\nabla_a \Psi|^n$, reflecting the shear-thinning behaviour. These limiting behaviours agree with those in [7], where the laminar model is analysed in more depth. The difference here though is that the limit $H_w \to \infty$ is not physically attained in the laminar regime: we transition to turbulent flow.

A. 2 Fully turbulent flows

For the fully turbulent regime, in [35] we use the Dodge–Metzner relation, which translates into the following equation defining $H_w \leftrightarrow Re_p$:

$$Re_p = H_w^{1-\frac{n}{2}} 6^{1-n} 2^{1-\frac{n}{2}} \left[\frac{4.0}{n'^{0.75}} \log \left(6^{1-n'} 2^{1-\frac{n'}{2}} E^{\frac{n'}{n}} H_w^{\frac{n'}{n}-\frac{n'}{2}} \right) - \frac{0.395}{n'^{1.2}} \right]^{2-n}, \tag{65}$$

where the generalized power-law index $n'(n, y_Y)$ is

$$n'(n, y_Y) = n(1 - y_Y) \frac{n y_Y + n + 1}{2n^2 y_Y^2 + 2n y_Y + n + 1} \tag{66}$$

for $y_Y = He/H_w$, which represents the dimensionless (effective laminar) plug width. Equation (65) must be solved iteratively for H_w if Re_p is specified, but defines Re_p explicitly if H_w is specified.

The function $\tau_w(|\nabla_a \Psi|)$ is found to increase monotonically in the turbulent regime. Considering He fixed (the rheology) and taking $H_w \to \infty$, we find $y_Y \to 0$, $n' \to n$ and $E \to 1$. Thus, we find that

$$Re_p \sim H_w^{1-\frac{n}{2}} \log H_w \quad \Rightarrow \quad |\nabla_a \Psi| \sim \sqrt{\tau_w} \left[\log \tau_w \right]^{1/(2-n)},$$

as $\tau_w \to \infty$. Thus, τ_w grows slightly less fast than $|\nabla_a \Psi|^2$, which would be the expectation in a fully rough turbulent regime, and the rheological dependency on n is minimal (in the exponent of the log term only), as would also be expected. Thus, we see essentially parallel curves in Fig. 5a at large H_w, independent of n.

A. 3 Transitional regimes

The transitional regime occurs between two critical values of the Metzner-Reed Reynolds number, $Re_{MR,1}(n, He/H_w)$ and $Re_{MR,2}(n, He/H_w)$ [35]. $Re_{MR,1}$ is the Reynolds number at which the flow is not laminar any more and $Re_{MR,2}$ is the Reynolds number at which the flow is fully turbulent. Between these values an interpolation is used based on the log of the friction factor. This results in a monotone variation in H_w vs Re_p, as seen in Fig. 5. $Re_{MR,1}(n, He/H_w)$ and $Re_{MR,2}(n, He/H_w)$ can be straightforwardly mapped into $H_{w,1}$ and $H_{w,2}$ that bound shear stress for transitional flows.

A. 4 Friction factor

In passing, we note that in hydraulics, it is common to express closures in terms of a friction factor f_f, defined as the ratio of wall shear stress to inertial stress scale. This can of course be done here, leading to

$$\mathbf{S} = \frac{r_a \rho f_f |\nabla_a \Psi|}{8H^3} \nabla_a \Psi.$$

In [35], the relevant expressions for f_f are given. For simpler fluids, such as power-law fluids, f_f is straightforward to evaluate across all regimes, and the Metzner–Reed Reynolds number has proven to be a useful tool. For more

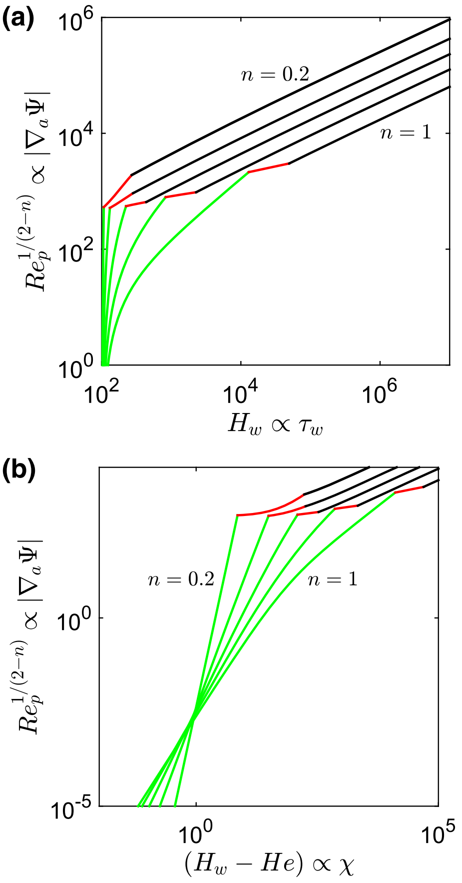

Fig. 5 The closure $H_w(Re_p)$ from [35], showing asymptotic behaviour: **a** $H_w \to \infty$; **b** $H_w \to He$. The closure is plotted for $He = 100$ and $n = 0.2,\ 0.4,\ 0.6,\ 0.8,\ 1$: *green*—laminar; *red*—transitional; *black*— turbulent. (Color figure online)

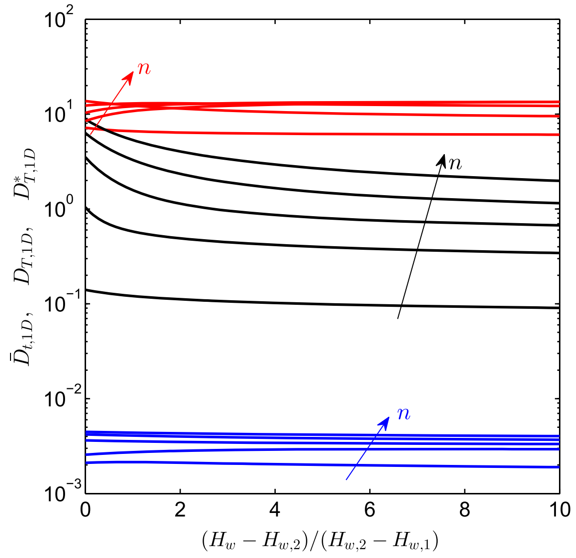

Fig. 6 Variation of $\bar{D}_{1D}$(*blue lines*), $D_{T,1D}$(*black lines*) and $D^*_{T,1D}$(*red lines*) with wall shear stress for $n = 0.2, 0.4, 0.6, 0.8$ and 1

complex fluids, the Metzner–Reed Reynolds number is not explicitly defined in terms of the process variables and f_f is just another level of algebraic complexity that obscures the essential mapping between local mean velocity (Re_p) and wall shear stress (H_w). The only advantage apparent to us in using f_f for Herschel–Bulkley fluids is a degree of familiarity with the friction-factor concept.

A. 5 Evaluating the Taylor dispersion terms

Similar to Sect. 1, we can find the averaged turbulent diffusivity and Taylor dispersion coefficients ($\bar{D}$, D_T, D_T^*) using the method introduced in [35]. We first construct the dimensional parameters, e.g.

$$\hat{D}_T = D_T \delta_0 \hat{r}_a \hat{\bar{W}}_0,$$

and then rescale it using the scaling defined in [35]. We eventually find

$$D_T = \frac{1}{2} |\nabla_a \Psi| D_{T,1D}, \tag{67}$$

where $D_{T,1D}$ is the dispersion coefficient obtained assuming a locally 1D channel flow [35]. Similar relations can be derived for $\bar{D}$ and D_T^*, i.e. multiplying the 1D results from [35] by $|\nabla_a \Psi|/2$.

It is worthwhile to compare the values of $\bar{D}_{1D}$, $D_{T,1D}$ and $D^*_{T,1D}$ (or equivalently $\bar{D}$, D_T and D_T^*). Figure 6 plots turbulent diffusivity and dispersion coefficients as a function of wall shear stress for fully turbulent flows. $H_{w,1}$ and $H_{w,2}$ are defined in Sect.1. As Fig. 6 shows, $\bar{D}$ is 2–3 orders of magnitude smaller than D_T. This is a typical feature of turbulent Taylor dispersion [42]. In addition, D_T^* is almost always larger than D_T. This is interesting, although the results computed so far have not revealed where these terms become important.

Appendix B: Variational principles

Equation (25) is an elliptic second-order equation, in which time evolution enters only via the fluid concentrations (see Sect. 3) or via flow rate changes. Here, we develop the variational theory relevant to solving (25) in a rectangle Ω with boundary $\partial\Omega_\Psi \bigcup \partial\Omega_S$, under which conditions (28) and (29), respectively are satisfied. We regard any suitably smooth $\tilde{\Psi}$ as an admissible stream function provided that (28) is satisfied. Similarly, $\tilde{\mathbf{S}}$ will be regarded as admissible provided that

$\nabla_a \cdot [\tilde{\mathbf{S}} + \mathbf{b}] = 0,$

and that (29) is satisfied. The following statements are easily proven using Green's theorem in the plane:

- For any admissible $\tilde{\Psi}$ & $\tilde{\mathbf{S}}$:

$$0 = \int_\Omega \tilde{\Psi} \nabla_a \cdot \mathbf{b} - \nabla_a \tilde{\Psi} \cdot \tilde{\mathbf{S}} \, \mathrm{d}\Omega + \int_{\partial\Omega_\Psi} \Psi_b \tilde{\mathbf{S}} \cdot \mathbf{n} \, \mathrm{d}s + \int_{\partial\Omega_S} \tilde{\Psi} f \, \mathrm{d}s. \tag{68}$$

- For Ψ & $\mathbf{S}$ that solve (25) with boundary conditions (28) and (29):

$$0 = \int_\Omega \Psi \nabla_a \cdot \mathbf{b} - \nabla_a \Psi \cdot \mathbf{S} \, \mathrm{d}\Omega + \int_{\partial\Omega_\Psi} \Psi_b \mathbf{S} \cdot \mathbf{n} \, \mathrm{d}s + \int_{\partial\Omega_S} \Psi f \, \mathrm{d}s. \tag{69}$$

- For the solution Ψ & $\mathbf{S}$, and any other admissible $\tilde{\Psi}$:

$$0 = \int_\Omega [\tilde{\Psi} - \Psi] \nabla_a \cdot \mathbf{b} - [\nabla_a \tilde{\Psi} - \nabla_a \Psi] \cdot \mathbf{S} \, \mathrm{d}\Omega + \int_{\partial\Omega_S} [\tilde{\Psi} - \Psi] f \, \mathrm{d}s. \tag{70}$$

- For the solution Ψ & $\mathbf{S}$, and any other admissible $\tilde{\mathbf{S}}$:

$$\int_\Omega \nabla_a \Psi \cdot [\tilde{\mathbf{S}} - \mathbf{S}] \, \mathrm{d}\Omega = \int_{\partial\Omega_\Psi} \Psi_b [\tilde{\mathbf{S}} - \mathbf{S}] \cdot \mathbf{n} \, \mathrm{d}s. \tag{71}$$

Now we consider the closure relationship defining $\mathbf{S}$, which is outlined in Appendix A. Provided that $|\nabla_a \Psi| > 0$ or equivalently $|\mathbf{S}| > r_a \tau_Y / H$, we can write this as

$$|\mathbf{S}|(|\nabla_a \Psi|) = \frac{r_a}{H} \tau_w(|\nabla_a \Psi|) = r_a \chi(|\nabla_a \Psi|) + \frac{r_a \tau_Y}{H}. \tag{72}$$

The function $\chi(|\nabla_a \Psi|)$ represents the contribution to the modified pressure gradient that is surplus to that needed to yield the fluid locally. It is continuous and strictly monotone. As the flow transitions through regimes, from laminar through to turbulent, the gradient of χ is continuous within any flow regime (but discontinuous when the flow transitions between regimes). Recall that $\chi(|\nabla_a \Psi|)$ also has a local dependency on (ϕ, ξ, t) through the local geometry and fluid concentrations present. However, in general we may represent $|\mathbf{S}|$ graphically (at any (ϕ, ξ, t)) as in Fig. 7a.

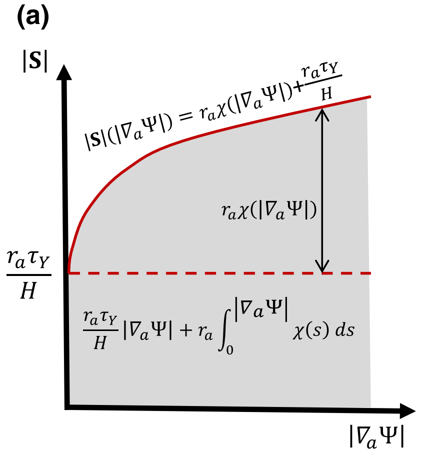

Fig. 7 **a** $|\mathbf{S}|(|\nabla_a\Psi|)$; **b** $|\nabla_a\Psi|(|\mathbf{S}|)$. The *shaded areas* contribute to the dissipation and potential functions. The *shaded areas* sum to $|\mathbf{S}||\nabla_a\Psi|$, used to establish Lemma 3

B. 1 Stream function and pressure potential functionals

The stream function potential functional $J(\tilde{\Psi})$ is defined as

$$J(\tilde{\Psi}) = \int_{\Omega}\int_0^{|\nabla_a\tilde{\Psi}|} |\mathbf{S}|(x)\,\mathrm{d}x - \tilde{\Psi}\nabla_a\cdot\mathbf{b}\,\mathrm{d}\Omega - \int_{\partial\Omega_S}\tilde{\Psi} f\,\mathrm{d}s, \tag{73}$$

which has the following property.

Lemma 1 *The solution Ψ minimizes $J(\tilde{\Psi})$ over all admissible $\tilde{\Psi}$.*

Proof We look at:

$$\begin{aligned}
J(\tilde{\Psi}) - J(\Psi) &= \int_{\Omega}\left(\int_{|\nabla_a\Psi|}^{|\nabla_a\tilde{\Psi}|}|\mathbf{S}|(x)\,\mathrm{d}x\right) - (\tilde{\Psi}-\Psi)\nabla_a\cdot\mathbf{b}\,\mathrm{d}\Omega - \int_{\partial\Omega_S}(\tilde{\Psi}-\Psi)f\,\mathrm{d}s\\
&= \int_{\Omega}\int_{|\nabla_a\Psi|}^{|\nabla_a\tilde{\Psi}|}|\mathbf{S}|(x)\,\mathrm{d}x\,\mathrm{d}\Omega - \int_{\Omega}[\nabla_a\tilde{\Psi}-\nabla_a\Psi]\cdot\mathbf{S}(|\nabla_a\Psi|)\,\mathrm{d}\Omega\\
&\geq \int_{\Omega}\int_{|\nabla_a\Psi|}^{|\nabla_a\tilde{\Psi}|}|\mathbf{S}|(x)\,\mathrm{d}x\,\mathrm{d}\Omega - \int_{\Omega}(|\nabla_a\tilde{\Psi}|-|\nabla_a\Psi|)|\mathbf{S}|(|\nabla_a\Psi|)\,\mathrm{d}\Omega\\
&= \int_{\Omega}\int_{|\nabla_a\Psi|}^{|\nabla_a\tilde{\Psi}|}(|\mathbf{S}|(x)-|\mathbf{S}|(|\nabla_a\Psi|))\,\mathrm{d}x \geq 0.
\end{aligned}$$

We have used (70) and then the Cauchy–Schwarz inequality above. In this last expression, note that $|\mathbf{S}|(x) > |\mathbf{S}|(|\nabla_a\Psi|)$ whenever $x > |\nabla_a\Psi|$ due to monotonicity. Thus, the sign of the integrant changes according to the limits and the integral is always positive. □

The minimization of $J(\tilde{\Psi})$ can also be expressed as a variational inequality, which is the basis of the augmented Lagrangian method used. Considering now Fig. 7b, we can define the function $|\nabla_a\Psi|(|\mathbf{S}|)$ by effectively inverting $|\mathbf{S}|(|\nabla_a\Psi|)$, as illustrated, i.e.

$$|\nabla_a\Psi|(|\mathbf{S}|) = \begin{cases} |\mathbf{S}|^{-1}(|\nabla_a\Psi|), & |\mathbf{S}| > \frac{r_a\tau_Y}{H},\\ 0, & |\mathbf{S}| \leq \frac{r_a\tau_Y}{H}.\end{cases}$$

We now define the pressure potential function $K(\tilde{\mathbf{S}})$ for any admissible $\tilde{\mathbf{S}}$ as follows.

$$K(\tilde{\mathbf{S}}) = -\int_{\Omega}\int_{\frac{r_a\tau_Y}{H}}^{|\tilde{\mathbf{S}}|} |\nabla_a\Psi|(y)\,\mathrm{d}y\,\mathrm{d}\Omega + \int_{\partial\Omega_\Psi} \Psi_b\tilde{\mathbf{S}}\cdot\mathbf{n}\,\mathrm{d}s. \tag{74}$$

Analogous to Lemma 1, we have the following.

Lemma 2 *The solution* $\mathbf{S}$ *maximizes* $K(\tilde{\mathbf{S}})$ *over all admissible* $\tilde{\mathbf{S}}$.

Proof We look at

$$\begin{aligned}
K(\mathbf{S}) - K(\tilde{\mathbf{S}}) &= \int_{\Omega}\int_{|\mathbf{S}|}^{|\tilde{\mathbf{S}}|} |\nabla_a\Psi|(y)\,\mathrm{d}y\,\mathrm{d}\Omega + \int_{\partial\Omega_\Psi} \Psi_b[\mathbf{S}-\tilde{\mathbf{S}}]\cdot\mathbf{n}\,\mathrm{d}s\\
&= \int_{\Omega}\int_{|\mathbf{S}|}^{|\tilde{\mathbf{S}}|} |\nabla_a\Psi|(y)\,\mathrm{d}y\,\mathrm{d}\Omega - \int_{\Omega} \nabla_a\Psi\cdot[\tilde{\mathbf{S}}-\mathbf{S}]\,\mathrm{d}\Omega\\
&\geq \int_{\Omega}\int_{|\mathbf{S}|}^{|\tilde{\mathbf{S}}|} |\nabla_a\Psi|(y)\,\mathrm{d}y\,\mathrm{d}\Omega - \int_{\Omega} |\nabla_a\Psi|(|\tilde{\mathbf{S}}|-|\mathbf{S}|)\,\mathrm{d}\Omega\\
&= \int_{\Omega}\int_{|\mathbf{S}|}^{|\tilde{\mathbf{S}}|} (|\nabla_a\Psi|(y)-|\nabla_a\Psi|)\,\mathrm{d}y\,\mathrm{d}\Omega \geq 0.
\end{aligned}$$

Here we have used (71) and then the Cauchy–Schwarz inequality. In the last expression, note that if $|\tilde{\mathbf{S}}| > |\mathbf{S}|$ then $|\nabla_a\Psi|(y) > |\nabla_a\Psi|$ due to monotonicity; similarly when $|\tilde{\mathbf{S}}| < |\mathbf{S}|$. Thus, the sign of the integrand changes according to the limits and the integral is always positive. □

Finally, since the shaded areas in Fig. 7a, b, sum to give $|\mathbf{S}||\nabla_a\Psi|$, we have

$$\int_{\Omega} |\mathbf{S}||\nabla_a\Psi|\,\mathrm{d}\Omega \int_{\Omega}\int_{0}^{|\nabla_a\Psi|} |\mathbf{S}|(x)\,\mathrm{d}x\,\mathrm{d}\Omega + \int_{\Omega}\int_{\frac{r_a\tau_Y}{H}}^{|\mathbf{S}|} |\nabla_a\Psi|(y)\,\mathrm{d}y\,\mathrm{d}\Omega,$$

which can be combined with (69). In combination with the above-mentioned minimization and maximization principles, we have the following minimax principle:

Lemma 3 *The solution pair* $(\mathbf{S}, \Psi)$ *satisfy*

$$K(\tilde{\mathbf{S}}) \leq K(\mathbf{S}) = J(\Psi) \leq J(\tilde{\Psi}),$$

for all admissible $\tilde{\mathbf{S}}$ *and* $\tilde{\Psi}$.

In the porous media context, similar variational principles are used to describe nonlinear filtration, e.g. [43,44]. The first (integral) terms in both $J(\cdot)$ and $K(\cdot)$ are referred to as *dissipation potentials*. In the porous media context, one is often more concerned with determining the pressure field, and a stream function formulation is restrictive in only applying to 2D flows. Thus, typically $K(\cdot)$ is referred to as the primal potential and $J(\cdot)$ as dual potential. Here however, we treat Lemma 1 as the primal principle as it leads to a unique stream function (see below). Note that the terminology *dissipation* results from (69) which is essentially a mechanical energy balance, equating the dissipation within the system to the work done by buoyancy forces and by the boundary terms.

B. 2 Existence and uniqueness

Lemma 1 is the basis of an existence and uniqueness result. Firstly, note that $J(\tilde{\Psi})$ can be split as follows:

$$\begin{aligned}
J(\tilde{\Psi}) &= \int_{\Omega} r_a\int_{0}^{|\nabla_a\tilde{\Psi}|} \chi(x)\,\mathrm{d}x\,\mathrm{d}\Omega + \int_{\Omega} \frac{r_a\tau_Y}{H}|\nabla_a\tilde{\Psi}|\,\mathrm{d}\Omega - \int_{\Omega} \tilde{\Psi}\nabla_a\cdot\mathbf{b}\,\mathrm{d}\Omega - \int_{\partial\Omega_S} \tilde{\Psi} f\,\mathrm{d}s,\\
&= J_0(\tilde{\Psi}) + J_1(\tilde{\Psi}) - L(\tilde{\Psi}).
\end{aligned} \tag{75}$$

The functional J_0 is strictly convex as the integrand has second derivative equal to the derivative of χ, which is a strictly monotone function. The functional J_1 containing the yield stress is convex, bit not strictly. Finally, L denotes the linear parts.

This problem structure is in a format where standard results may be applied (e.g. [45, Theorem 2.1, Chap. 5]), to guarantee the existence of a unique weak solution. The relevant function space is determined by the behaviour of J_0 as $||\tilde{\Psi}|| \to \infty$. From the analysis in Appendix A, we see that in the fully turbulent regime $|\nabla_a \Psi| \sim \sqrt{\tau_w}\left[\log \tau_w\right]^{1/(2-n)}$ as $|\nabla_a \Psi| \to \infty$, and therefore also

$$\chi\left[\log \chi\right]^{2/(2-n)} \sim |\nabla_a \Psi|^2.$$

This suggests $\chi \gtrsim |\nabla_a \Psi|^{2-\epsilon}$ for any small $\epsilon > 0$ as $|\nabla_a \Psi| \to \infty$, i.e. the log term is less significant than any power.

Proceeding now as in [10], we can infer that $\Psi \in W^{1,3-\epsilon}(\Omega)$, with further details specific to the boundary conditions to be considered. It is interesting to compare with the results for the purely laminar case considered in [10], where the growth of χ using only the laminar closure resulted in $\Psi \in W^{1,1+n_{\min}}(\Omega)$. It appears that the turbulent closure results in a smoother weak solution and a function space largely independent of the rheology.

B. 3 Pressure formulation and stress maximization

The maximization of $K(\tilde{\mathbf{S}})$ leads to an equality as the optimality condition. The resulting partial differential equation (for the pressure) does not, however, uniquely determine $\mathbf{S}$, where the flow is stationary. We may derive the pressure equation directly by reorganizing (22) to eliminate Ψ instead of p:

$$0 = \nabla_a \cdot \left[r_a^2 \frac{|\nabla_a \Psi|(|\mathbf{S}|)}{|\mathbf{S}|} \left(\nabla_a p + \mathbf{b}_p\right)\right], \tag{76}$$

$$\mathbf{b}_p = \frac{\rho - 1}{Fr^2}\left(-\sin\beta \sin\pi\phi, \cos\beta\right), \tag{77}$$

$$|\mathbf{S}| = \left|\left(-r_a \frac{\partial \bar{p}}{\partial \xi} - \frac{r_a(\rho-1)\cos\beta}{Fr^2}, \frac{\partial \bar{p}}{\partial \phi} - \frac{r_a(\rho-1)\sin\beta\sin\pi\phi}{Fr^2}\right)\right|. \tag{78}$$

The function $|\nabla_a \Psi|(|\mathbf{S}|)$ is qualitatively illustrated in Fig. 7b.

References

1. Guillot D, Nelson E (2006) Well Cementing. Schlumberger Educational Services, Sugar Land
2. Brice JW Jr, Holmes BC (1964) Engineered casing cementing programs using turbulent flow techniques. J Petrol Technol 16:503–508
3. Couturler M, Guillot D, Hendriks H, Callet F (1990) Design rules and associated spacer properties for optimal mud removal in eccentric annuli. In: CIM/SPE international technical meeting. Society of Petroleum Engineers paper 21594
4. Jamot A (1974) Déplacement de la boue par le latier de ciment dans l espace annulaire tubage-paroi d un puits. Revue Assoc. Franc. Techn. Petr 224:27–37
5. Lockyear CF, Ryan DF, Gunningham MM (1990) Cement channeling: how to predict and prevent. Society of Petroleum Engineers, SPE paper 19865
6. Bittleston SH, Ferguson J, Frigaard IA (2002) Mud removal and cement placement during primary cementing of an oil well-Laminar non-Newtonian displacements in an eccentric annular Hele-Shaw cell. J Eng Math 43:229–253
7. Pelipenko S, Frigaard IA (2004) Two-dimensional computational simulation of eccentric annular cementing displacements. IMA J App Math 69:557–583
8. Carrasco-Teja M, Frigaard IA, Seymour BR, Storey S (2008) Viscoplastic fluid displacements in horizontal narrow eccentric annuli: stratification and travelling wave solutions. J Fluid Mech 605:293
9. Pelipenko S, Frigaard IA (2004) On steady state displacements in primary cementing of an oil well. J Eng Math 46:1–26
10. Pelipenko S, Frigaard IA (2004) Visco-plastic fluid displacements in near-vertical narrow eccentric annuli: prediction of travelling-wave solutions and interfacial instability. J Fluid Mech 520:343–377

11. Bogaerts M, Azwar M, Dooply M, Salehpoor A (2015) Well cementing: an integral part of well integrity. In: Offshore Technology Conference Brasil, Rio de Janeiro, Brazil, 27th–29th October 2015. OTC-26314-MS
12. Gregatti A, Carvalho G, Piedade T, Campos G (2015) Cementing in front of saline zone and carbonate reservoir with presence of CO_2. In: OTC Brasil
13. Guo Y, Qi J, Zheng YS, Taoutaou S, Wang R, An Y, Guo H (2015) Cementing optimization through an enhanced ultrasonic imaging tool. SPE paper 176069-MS
14. Osayande V, Isgenderov I, Bogaerts M, Kurawle I, Florez P (2004) Beating the odds with channeling in erd well cementing: solution to persistent channeling problems. Society of Petroleum Engineers, SPE paper 171271-MS
15. Watson TL (2004) Surface casing vent flow repair-a process. In: Canadian International petroleum conference, Calgary, Alberta, 8th-10th June 2004. PETSOC-2004-297
16. McLean RH, Manry CW, Whitaker WW (1967) Displacement mechanics in primary cementing. Society of Petroleum Engineers, SPE paper 1488
17. Allouche M, Frigaard IA, Sona G (2000) Static wall layers in the displacement of two visco-plastic fluids in a plane channel. J. Fluid Mech. 424:243–277
18. Frigaard IA, Leimgruber S, Scherzer O (2003) Variational methods and maximal residual wall layers. J Fluid Mech 483:37–65
19. Wielage-Burchard K, Frigaard IA (2011) Static wall layers in plane channel displacement flows. J Non-Newt Fluid Mech 166:245–261
20. Zare A, Roustaei A, Frigaard IA (2017) Buoyancy effects on micro-annulus formation: Newtonian-bingham fluid displacements in vertical channels. J Non-Newt Fluid Mech (submitted)
21. Alba K, Taghavi SM, Frigaard IA (2013) Miscible density-unstable displacement flows in inclined tube. Phys Fluids 25:067101
22. Taghavi SM, Alba K, Seon T, Wielage-Burchard K, Martinez DM, Frigaard IA (2012) Miscible displacement flows in near-horizontal ducts at low atwood number. J Fluid Mech 696:175–214
23. Moyers-Gonzalez MA, Frigaard IA (2008) Kinematic instabilities in two-layer eccentric annular flows, part 1: Newtonian fluids. J Eng Math 62:103–131
24. Moyers-Gonzalez MA, Frigaard IA (2009) Kinematic instabilities in two-layer eccentric annular flows, part 2: shear-thinning and yield-stress effects. J Eng Math 65:25–52
25. Dusseault MB, Jackson RE, Macdonald D (2014) Towards a road map for mitigating the rates and occurrences of long-term wellbore leakage. University of Waterloo and Geofirma Engineering LTD, Waterloo
26. Watson TL, Bachu S (2008) Identification of wells with high CO_2-leakage potential in mature oil fields developed for CO_2-enhanced oil recovery. In: SPE symposium on improved oil Recovery. Society of Petroleum Engineers
27. Watson TL, Bachu S (2009) Evaluation of the potential for gas and CO_2 leakage along wellbores. SPE Drill. Complet. 24:115–126
28. Carrasco-Teja M, Frigaard IA (2010) Non-Newtonian fluid displacements in horizontal narrow eccentric annuli: effects of slow motion of the inner cylinder. J Fluid Mech 653:137–173
29. Tardy PMJ, Bittleston SH (2015) A model for annular displacements of wellbore completion fluids involving casing movement. J Pet Sci Eng 126:105–123
30. Chung SY, Rhee GH, Sung HJ (2002) Direct numerical simulation of turbulent concentric annular pipe flow—Part 1: flow field. Int J Heat Fluid Flow 23:426–440
31. Freund JB, Lele SK, Moin P (2000) Compressibility effects in a turbulent annular mixing layer. Part 1. Turbulence and growth rate. J Fluid Mech 421:229–267
32. Nikitin N, Wang H, Chernyshenko S (2009) Turbulent flow and heat transfer in eccentric annulus. J Fluid Mech 638:95–116
33. Nouri JM, Whitelaw JH (1997) Flow of Newtonian and non-Newtonian fluids in an eccentric annulus with rotation of the inner cylinder. Int J Heat Fluid Flow 18(2):236–246
34. Sawko RAC (2012) Mathematical and computational methods of non-Newtonian, multiphase flows. Ph.D. Thesis, Cranfield University
35. Maleki A, Frigaard IA (2016) Axial dispersion in weakly turbulent flows of yield stress fluids. J Non-Newt Fluid Mech 235:1–19
36. Dodge DW, Metzner AB (1959) Turbulent flow of non-Newtonian systems. AIChE J 5:189–204
37. Dodge DW, Metzner AB (1962) Errata. AIChE J 8:143
38. Metzner AB, Reed JC (1955) Flow of non-Newtonian fluids: correlation of the laminar, transition, and turbulent-flow regions. AIChE J 1:434–440
39. Taghavi SM, Frigaard IA (2013) Estimation of mixing volumes in buoyant miscible displacement flows along near-horizontal pipes. Can J Chem Eng 91:399–412
40. Zhang J, Frigaard IA (2006) Dispersion effects in the miscible displacement of two fluids in a duct of large aspect ratio. J Fluid Mech 549:225–251
41. Fowler AC (1998) Mathematical models in the applied sciences. Cambridge University Press, Cambridge
42. Taylor GI (1954) The dispersion of matter in turbulent flow through a pipe. Proc R Soc Lond A 223:446–468
43. Barenblatt GI, Entov VM, Ryzhik VM (1989) Theory of fluid flows through natural rocks. Kluwer Academic, Dordrecht
44. Spena FR, Vacca A (2001) A potential formulation of non-linear models of flow through anisotropic porous media. Transp Porous Med 45(3):405–421
45. Glowinski R (1984) Numerical methods for nonlinear variational problems. Springer, New York